行政院國家科學委員會專題研究計畫成果報告

同調控制超快光學技術與凝態材料聲子動力學研究

計畫類別：☑個別型計畫　□整合型計畫

計畫編號：NSC 90 —2112—M009—052

執行期間：90 年 8 月 1 日至 91 年 7 月 31 日

個別型計畫：計畫主持人：黃中垚
共同主持人：

整合型計畫：總計畫主持人：
子計畫主持人：

註：整合型計畫總報告與子計畫成果報告請分開編印各成一冊，彙整一起繳送國科會。

處理方式：☑可立即對外提供參考
（請打∨）□一年後可對外提供參考
□兩年後可對外提供參考
（必要時，本會得展延發表時限）

執行單位：國立交通大學光電工程研究所

中華民國　　年　　月　　日

同調控制超快光學技術與凝態材料聲子動力學研究

計劃編號: NSC90-2112-M-009-052

執行期限: 民國九十年八月一日至九十一年七月三十一日

主持人: 黃中垚

傳真: 03-5716631

電子郵遞地址: jyhuang@cc.nctu.edu.tw

執行機關: 交通大學光電工程研究所

摘要

在本研究期間，我們成功的建立一些可用於分析凝態材料動態之超快線性與非線性光學分析技術。其中光穿透/反射微量變化分析儀為研究晶體與量子侷限樣品之晶格聲子動態之利器。利用四倍焦矩無色散之超快光脈衝整形系統可控制光與材料交互作用。我們將 Gerchberg-Saxton 演算法加入飛秒脈衝整形控制迴路，而發展出經精確設計之光脈衝波串，可應用於同調控制之凝態動力學研究。

具適應性之光脈衝整形系統是控制複雜的超快雷射與凝態材料交互作用的可行方法。為達此目的，我們將演化策略演算法加入此脈衝整形控制迴路，証明經九十代的演化演算，此一脈衝整形裝置可將已變形之脈衝恢復至富氏轉換極限之波形。

非線性光學診斷方法常受限於低的信號產生效率。例如具頻率鑑別性之光閘分析技術(FROG)常使用二倍頻產生過程作為光場自相關計算機制。因此 FROG 不適用於分析微弱光信號之實驗。我們結合光參量放大過程和 FROG 技術，發展出全光場分析系統，具有對紅外光之靈敏性和達 10 atto joules 的偵測靈敏度的雙重優點。我們也設計適合單脈衝量測之 OPA-FROG 系統，以為未來凝態材料動力學研究之所需。

Probing the Phonon Dynamics of Condensed-Phase Materials with Coherent Control Ultrafast Optical Techniques

NSC90-2112-M-009-052 (Aug. 1, 2001 to July 31, 2002)

Investigator: Jung Y. Huang

Organization: Institute of Electro-Optical Engineering

Chiao Tung University

Hsinchu, Taiwan 30050, R.O.C.

Tel: 03-5719755

Fax: 03-5716631

E-mail: jyhuang@cc.nctu.edu.tw

Abstract

In this research, we have successfully developed and established some highly useful ultrafast linear and nonlinear optical techniques for probing the dynamics of condensed-phase materials. The differential reflectivity/transmission apparatus offers unique opportunity to study the lattice dynamics of crystalline samples in bulk or in dimensional confinement systems. Ultrafast pulse-shaping technique based on a 4*f* dispersion-free apparatus is developed to offer the capability for controlling ultrafast laser material interaction. We implement Gerchberg-Saxton algorithm in a phase-only femtosecond pulse shaper for an efficient and accurate pulse design. Based on the FROG pattern analysis, we show that this method can be used to generate an ultrafast pulse train with a user-specific profile for coherent control experiment. This is highly useful for the

study of coherent phonon dynamics in advanced materials for novel applications.

For the control on more complicated ultrafast laser material interaction, an adaptive pulse shaper may be the correct approach. To allow the investigation into such research topics, we implement evolution strategy algorithm into the femtosecond laser pulse shaping apparatus with a LC-SLM phase modulating device. We show that in 90 generations, the apparatus can compensate the phase distortion of a distorted pulse and bring it back to transform-limited profile. This apparatus is therefore useful for mapping a specific molecule in an inhomogeneous environment by properly training the adaptive feedback loop.

The applicability of nonlinear optical methodology is often limited owing to its low signal strength. A second-harmonic autocorrelator is usually implemented in a FROG-based ultrafast laser diagnostic system. This becomes problematic in use of FROG technique for an experimental detection. We develop an OPA-FROG to solve this difficulty. OPA is used to provide an appreciable gain for a weak optical input signal and therefore FROG pattern analysis can reliably proceed. We show the OPA-FROG can achieve a detection limit as low as 10 atto Joule, which corresponds to 30 photons in single pulse. An extension to single-shot version of the OPA-FROG is proposed for the future study.

Contents

I. Introduction

Phonons and their interactions play an important role in the fields of solid state physics, solid-state optoelectronics, superconductivity, and thermoelectrics. As an illustration with polar semiconductors such as GaAs, ZnSe, and GaN, *etc.*, the electron mobility and dynamical processes are known to be limited by the interaction of longitudinal optical (LO) phonons with charge carriers. The resulting saturation velocity ($v_{sat}=2\times10^7$ cm/sec in GaAs) of the charge carriers in the presence of an external electric field are therefore ruled by the rate of the electrons emitting LO phonons [1]. This velocity determines how fast a semiconductor microelectronic device can operate ($t_r=L_{gate}/v_{sat}$).

In an optoelectronic device such as intersubband lasers the carriers are usually injected from a barrier layer into an active quantum well and must lose at least 100-meV energy before be captured by quasi-bound states and then join the lasing process. The injected carriers thermalize by emitting LO phonons [2]. In a quantum confined structure, the density of states of LO phonons is modified and the phonons emitted by the carriers could deviate significantly from equilibrium. It is highly probable for these "hot" phonons to be reabsorbed by the charge carriers [3]. The re-absorption impedes the thermalization of the injected carriers and therefore decreases the modulation speed of laser. This phenomenon, which often occurs in quantum-confined structures, is called hot phonon bottlenecking. In some materials, the emitted phonons can couple to acoustic phonons via Klemens' channel [4]. The energy taken away by acoustic phonons can not be recovered and therefore accelerates the thermalization process of the injected carriers.

Phonon interactions also yield numerous novel mechanisms. A representative example lies in the BCS theory of superconductivity. Two electrons are proposed to form a Cooper pair (Boson) via mediating interaction produced by phonons [5].

In a nanostructured material, the effects of dimensional confinement on the phonon

modes can alter phonon interactions. The continuous wavevector q_z of phonons in a bulk material becomes restricted to integral multiples of $q_z = \pi/L_z$ in a nanostructure. Such dimensional confinement-induced phase space restriction suggests the carrier-phonon interactions will be modified by the phonon confinement, thus opens up much unexplored research territories. One of such territories is thermoelectrics.

When a current flows through a pair of n-type and p-type semiconductors connected in series, the electrons in the n-type material and the holes in the p-type material all carry heat away from the junction, which leads to a cooling effect [6]. The reverse process can be used as a thermo-to-electrical energy conversion engine. Although the device possesses numerous attractive features, TE devices had only been used in niche areas owing to their poor efficiency. The figure of merit of TE effect usually represents through a figure of merit parameter ZT with $Z=S^2\sigma/\kappa$ and T the temperature [6]. Here $S= -V/\Delta T$ denotes the Seeback coefficient, σ the electrical conductivity, and κ the thermal conductivity. Thus material suited for TE application shall be both good electrical conductor and thermal insulator. This goal may be achieved by reducing the phonon thermal conductivity without sacrificing much the electrical conductivity. Dimensional confinement can be implemented to engineering phonon and electron transport properties independently by improving the electric power factor $S^2\sigma$ and reducing the phonon thermal conductivity κ separately. The nonequilibrium phonon transport in nanostructure is a very interesting issue that calls for further study. The issue can be probed with fast laser material interactions.

In this annual report, we present the development and assembly of ultrafast laser techniques and knowledge resources needed for investigating the above mentioned topics. Section II the physics of coherent phonon generation and instrument used to probe the coherent phonon with femtosecond laser are described. Preliminary experimental results

on ZnSe epitaxial film on GaAs(001) and colloid solution of CdSe quantum dots are shown. To coherently control the phonon excitation, technique with femtosecond pulse shaping is detailed in Section III. Finally in Sec. IV, a complete field diagnostic tool is described for characterizing femtosecond optical signal with extremely weak intensity. Primitive study on the optical parametric amplification (OPA)-based frequency resolved optical gating (FROG) technique has demonstrated that a sensitivity as low as 10 atto Joules (5 photons only) can be achieved. This research is to be continued into the second phase. Interesting topics for the future study are discussed in the concluding section.

References of Section I

[1] T. A. Fjeidly, T. Ytterdal, and M. S. Shur, *Introduction to Device Modeling and Circuit Simulation*, Chap. 2 (Wiley, New York 1998). J. Singh, *Semiconductor Devices*, Chap. 4 *Carrier Dynamics in Semiconductor.*

[2] D. S. Chemla and J. Shah, *Ultrafast dynamics of many-body processes and fundamental quantum mechanical phenomena in semiconductors,* Proc. Natl. Acad. Sci. 97, 2437 (2000).

[3] J. Urayama *et al.*, *Observation of Phonon Bottleneck in Quantum Dot Electronic Relaxation,* Phys. Rev. Lett. 86, 4930 (2001).

[4] A. Debernardi, *et al.*, *Anharmonic Phonon Lifetimes in Semiconductors from DFT,* Phys. Rev. Lett. 75, 1819 (1995).

[5] S. V. Vonsovsky and M. I. Katsnelson, *Quantum Solid-State Physics*, Chap. 5 (Springer-Verlag, Berlin, 1989).

[6] G. Chen and A. Shakouri, *Heat Transfer in Nanostructures*, Trans. of the ASME, 124, 242 (2002).

II. Coherent Phonon Generation with Femtosecond Laser Pulses

2.1 Advantages of Impulsive Coherent Phonon Spectroscopy

There exist two types of collective excitation in a crystal lattice: The acoustic phonon modes represent distortions (compression/expansion) of unit cells. The collective excitation is called "longitudinal" or "transverse" depending upon whether the distortion is parallel or perpendicular to the wave vector of the collective excitation (see Fig. 2.1.1(a)).

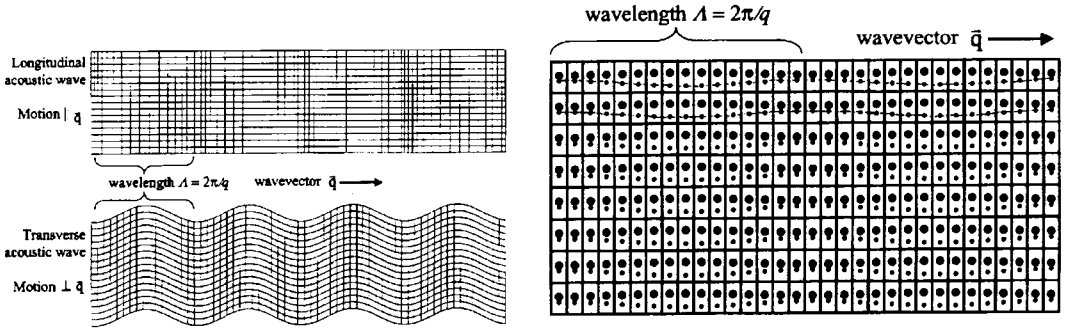

Fig. 2.1.1 Schematic showing the relative displacement in (a, LH) acoustic phonon modes (LA and TA), and (b, RH) optic phonon mode (TO) excitations.

The second type of collective lattice excitation is called "optic phonon". Optic phonon excitation generates only vibrations of ions or molecules against each other in unit cell (Fig. 2.1.1(b)). No change in unit cell size or shape can be observed. Collective phonon excitations, which produce the same distortions as the structural change during the phase transition of a crystalline solid, could be influenced significantly by the structural phase transition. The vibration frequencies of these phonon modes often decrease as the temperature is increased near to the phase transition and exhibits a phonon softening effect [2]. This phenomenon can be observed clearly with time domain techniques as shown in Fig. 2.1.2 on a ferroelectric crystal RD_2PO_4.[3]

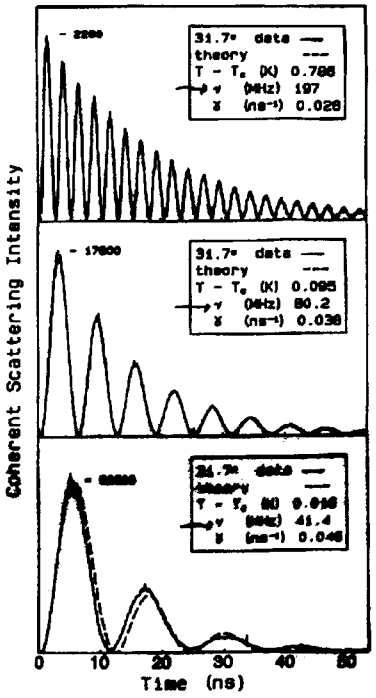

Fig. 2.1.2 Impulsive stimulated Rayleigh scattering in a RD_2PO_4 crystal near to its ferroelectric-paraelectric phase transition (reproduced from [3])

Although frequency-domain light scattering spectroscopy can also be employed to probe the structural phase transition, the following limitations restrict its applicability: Brillouin peaks with frequencies below 0.5-1 GHz (1 cm^{-1}=29.929 GHz=0.124 meV) are often buried below parasitically scattered laser light background. For acoustic phonon modes related to the structural phase transition are strongly damped and therefore merge in central peak and overlap with other slow relaxation modes (see Fig. 2.1.3) [4]. Time domain techniques with pico- to femtosecond laser pulses avoid such difficulties. In addition, numerous coherent approaches associated with ultrafast laser technologies can also be employed to control and identify the underlying phonon dynamical process.

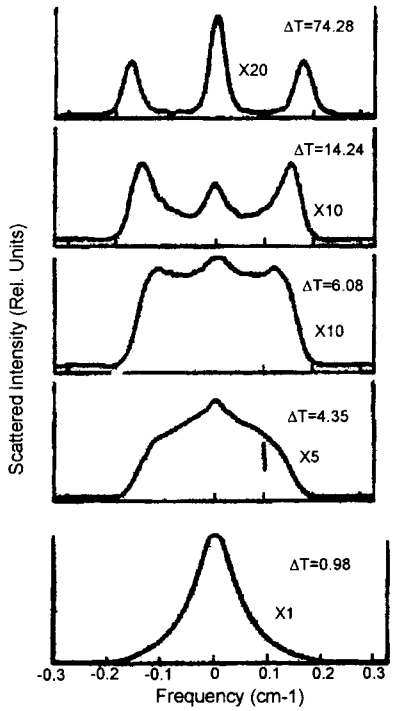

Fig. 2.1.3 Frequency-domain light scattering spectra of RD_2PO_4 crystal (from top to bottom: temperature increases toward the phase transition temperature. Figure is reproduced from [4])

2.2 Mechanisms of Coherent Phonon Generation

Ultrafast laser-material interaction can be employed to generate coherent phonons via two basic mechanisms [5]. When the incident photon energy is below the material bandgap, the phonons of the transparent sample can be produced by impulsive stimulated Raman scattering (ISRS) process. The ions at the equilibrium positions in unit cell impulsively acquire a velocity v (t=0)=v_0 from the ultrafast laser-material interaction. The impulsive force from ISRS can be derived to be

$$f(q,t) = -\partial U/\partial Q = \alpha' F(q,t)$$
$$with \quad U = -\frac{1}{8\pi}\frac{\partial \alpha}{\partial Q}\Big|_{Q_0} \cdot Q(q,t) E^2_{laser}(t) \cdot \tag{1}$$

Here the phonon amplitude $Q(q, t)$ can be expressed as

$$Q(q,t) = \int_{-\infty}^{\infty} G(q,t-t')\alpha' F(q,t')dt' , \tag{2}$$

and with an impulsive excitation, $Q(q, t)$ can be further simplified as

$$Q(q,t) = \int_{-\infty}^{\infty} G(q,t-t')\alpha' F_0(q)\delta(t')dt' = \alpha' F_0(q)G(q,t). \tag{3}$$

Here $G(q, t)$ denotes the Green function and can be solved from the following equation:

$$\left[\frac{\partial^2}{\partial t^2} + 2\gamma(q)\frac{\partial}{\partial t} + \Omega_0^2(q)\right] G(q,t) = \frac{\delta(t)}{m}$$
$$with \quad G(q,t) = \frac{e^{-\gamma t}\sin(\Omega t + \phi)}{m\Omega(q)} = \frac{e^{-\gamma t}\sin(\Omega t + \phi)}{m\sqrt{\Omega_0^2(q) - \gamma^2(q)}} \tag{4}$$

When the incident photon energy is higher than the material bandgap, the charge carriers are produced via ultrafast interband transitions. The Coulomb interaction experienced by the ions is shielded by the optically generated carriers and therefore new equilibrium position is produced for each ion $Q(t=0)=Q_0$. This leads to a phonon amplitude of $Q(t)=Q_0\cos(\Omega t+\phi)$ from displacive excitation of coherent phonon (DECP) process. Rich information could be gained since both the charge carriers and coherent phonon be generated within very short period. Electron-phonon coupling may be detected. Particularly interesting is the coupling may be altered in a dimensional-confined system such as semiconductor quantum dots.

2.3 Experimental Setup

The excitation of coherent phonon alters the index modulation and therefore can yield a small change in optical reflectivity. The differential reflectivity signal $\Delta R/R$ can be as small as 10^{-6} in reflection and 10^{-4} in transmission [6]. Sophisticated signal processing shall be employed in order to achieve such high detection sensitivity. Fig. 2.3.1 depicts the schematic of the experimental setup used to achieve this sensitivity. Pump laser beam is modulated with an optical chopper and a piezoelectric shaker was employed to deduce the time-derivative differential reflectivity signal $\partial(\Delta R/R)/\partial t$. A combination of a

Walloston prism and a split photodiode is employed to probe the pump-induced depolarization and therefore yields pump-induced optical anisotropy while avoids the influence of pump intensity fluctuation. Time delay is controlled via a stepper motorized translation stage with a precision of 1 μm. This setup can be used to probe not only the A_{1g}-symmetry phonon modes but also the E_g-symmetry modes.

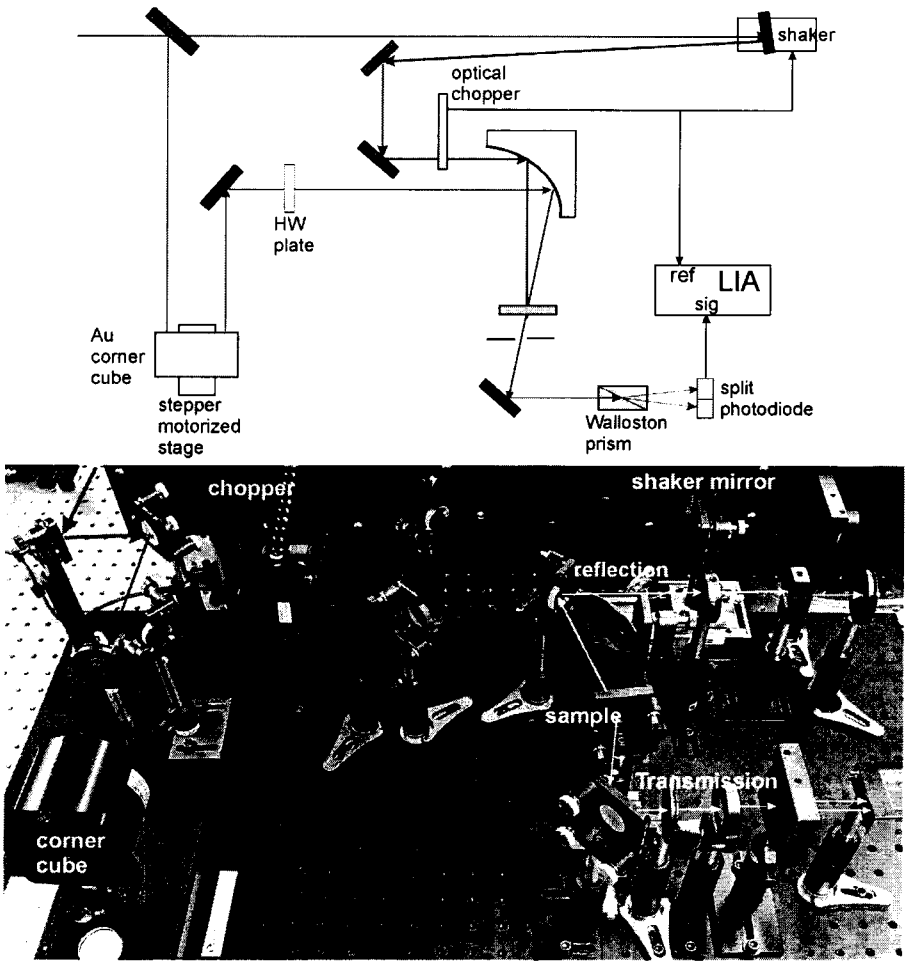

Fig. 2.3.1 (a: top) Schematic and (b: bottom) real setup of the femtosecond differential reflectivity measurement apparatus

2.4 Some Preliminary Results

2.4.1 ZnSe epitaxial layer on GaAs(001)

The relaxation of photoexcited carriers in semiconductors is often via the emission of

longitudinal optical phonon. Frohlich coupling constant presents the strength of electron-phonon interaction α. In GaAs, the Frohlich constant is about 0.06 and therefore belongs to the weak electron-phonon coupling systems. For ZnSe, the α parameter is 0.47, indicating a strong coupling between electron and optical phonons [7]. As illustrated in Introduction Section, the electron mobility and dynamical processes in polar semiconductors are limited by the interaction of longitudinal optical (LO) phonons with charge carriers. It is therefore interesting to know how the dynamics of longitudinal optical phonons varies with the generation of charged carriers.

ZnSe was epitaxially grown on GaAs(001) substrate with a MBE system. The resulting films exhibit a major PL peak at 458 nm when they are excited at 435 nm (see Fig. 2.4.1).

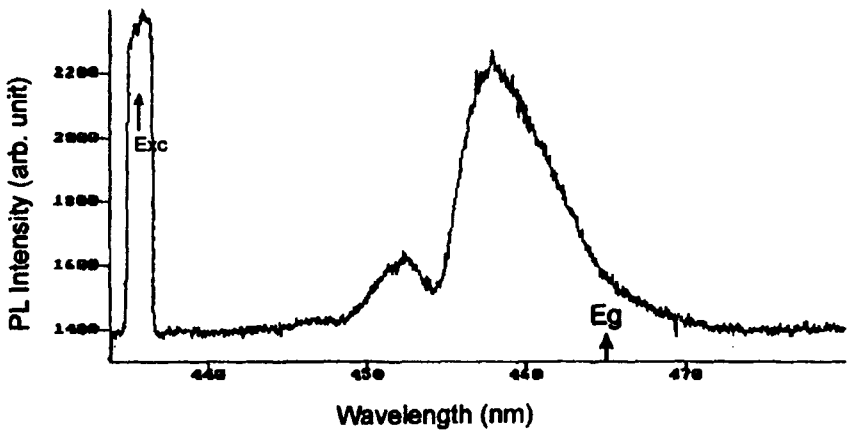

Fig. 2.4.1 Photoluminescence spectrum of ZnSe film excited at 435 nm.

ZnSe belongs to the $\bar{4}3m$ group and possesses one independent component $\chi_{41}^{(2)}$ in its second-order optical susceptibility tensor. When the film is subjected to the excitation of a s-polarized laser beam, the reflected p-polarized second-harmonic field is proportional to the effective optical susceptibility

$$\chi_{eff}^{(2)}(s \to p) = \sum_{ijk} \hat{e}_i(2\omega) \cdot [\chi_{ijk}^{(2)} : \hat{e}_j(\omega)\hat{e}_k(\omega)]$$
$$= -\frac{1}{2}\chi_{41}^{(2)} \sin\theta \sin(2\Phi) \tag{2.4.1}$$

where ϑ denotes the incident angle of the laser beam and Φ the angle between the [100]-axis of the ZnSe crystalline film and the incident plane. Similarly the *p*-polarized SH signal excited by a *p*-polarized pump can be derived to be

$$\chi_{eff}^{(2)}(p \to p) = \sum_{ijk} \hat{e}_i(2\omega) \cdot [\chi_{ijk}^{(2)} : \hat{e}_j(\omega)\hat{e}_k(\omega)]$$
$$= -\frac{1}{2}\chi_{41}^{(2)} \cos^2\theta \sin\theta \sin(2\Phi) \tag{2.4.2}$$

The second harmonic generation was employed to probe how the second-order optical susceptibility in a polar semiconductor changes with photoexcited carriers. A 150-*fs* laser beam with a wavelength of 455 nm perpendicularly incidents on a ZnSe film and produces charged carriers and after various delay times, a fundamental beam at 916 nm incidents on the sample at 45° to probe the photoexcited film with second-harmonic generation. The results are presented in Fig. 2.4.2.

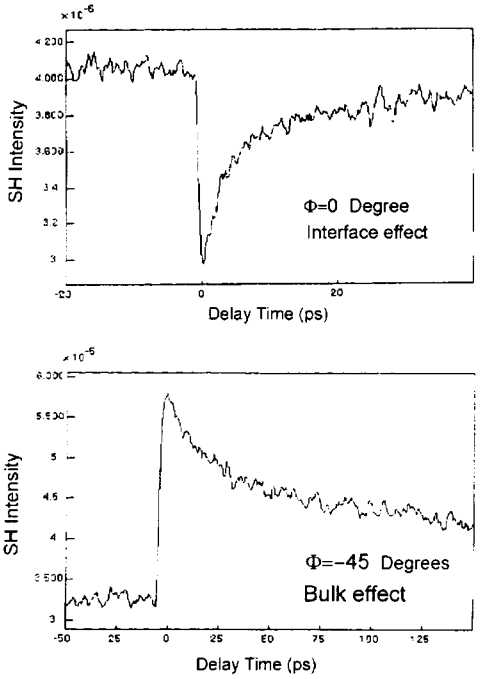

Fig. 2.4.2 The *p*-in *p*-out second harmonic signal reflected from a ZnSe film at (top) Φ=0° and (bottom) Φ=45° from the [100] axis of the film.

The second harmonic signal generated at Φ=0 is mainly from the heterojuction interface of ZnSe/GaAs where significant lattice distortion can occur. No SH signal from the bulk shall be observed owing to the sin[2Φ]-azimuthal dependence of ZnSe. The pump-induced reduction in SHG was detected. The signal reduction can be either originated from the screening effect of carriers on the interfacial nonlinearity or the reduced SHG transition caused by the final state occupation. Further work on SHG spectroscopy with various fundamental wavelengths is currently undertaking.

When the sample is rotated to Φ=45°, the SHG signal generated shall come from the bulk of the film. The two relaxation times can be observed with a faster one at 10 *ps* and the slower one at 100 *ps*. We define a photo-induced SHG change by $\Delta I(2\omega) = I_{2\omega}(pump \neq 0) - I_{2\omega}(pump = 0)$.

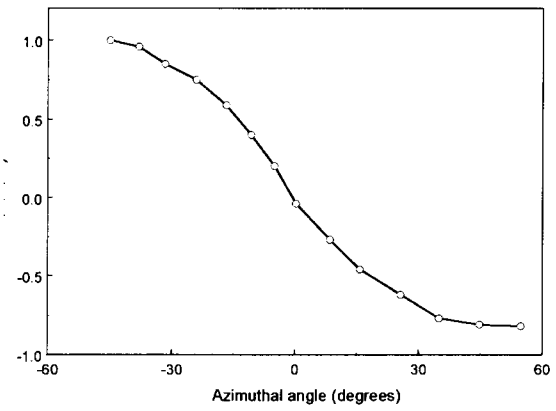

Fig. 2.4.3 Pump-induced SHG changes plotted as a function of the angle between the [100]-axis of the ZnSe crystalline film and the incident plane.

It is interesting to know that the SHG difference exhibits Sin (2Φ) azimuthal pattern (Fig. 2.4.3), indicating that the spatial distribution of the photoexcited carriers shall also follow the bonding structure of the crystalline film. The time-resolved SHG with better temporal resolution shall yield much more detail information about the dynamics of charged carrier-

longitudinal phonon coupling.

We employed the differential transmission EO sampling apparatus shown in Fig. 2.3.1 for probing the longitudinal phonon dynamics of ZnSe/GaAs (001). The femtosecond laser is 40 *fs* pulse at 800 nm (1.55 eV), which is far below the bandgap of the film (2.67 eV). Therefore the phonon generation mechanism shall originate from impulsive stimulated Raman scattering (ISRS) process. Figure 2.4.4 present the observed coherent phonon dynamics with a relaxation time of about 1 *ps*.

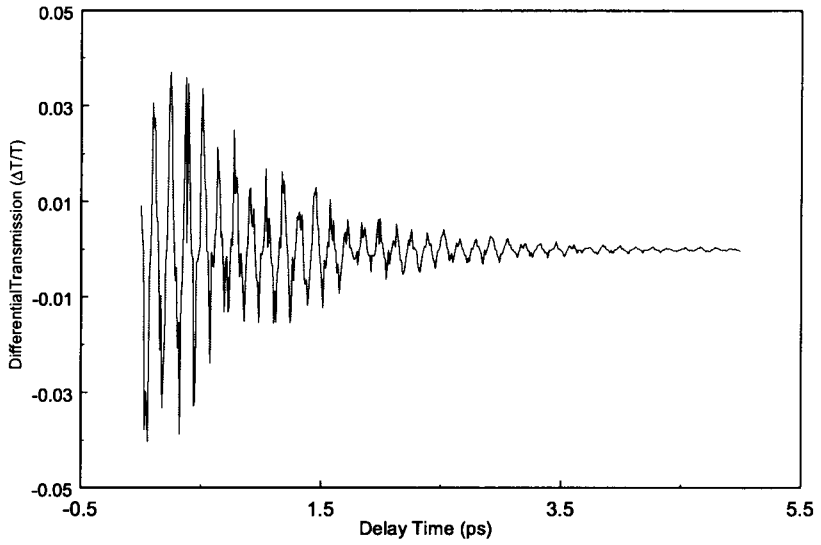

Figure 2.4.4 The observed differential transmission signal as a function of delay time to reflect the coherent longitudinal optical phonon dynamics in ZnSe/GaAs(001) sample.

This LO phonon relaxation is via a coupling from LO to acoustic phonons and shall be temperature sensitive. The LO phonon frequency can be deduced by fast Fourier transform the time-resolved curve of phonon oscillation and was found to be ω_{LO}=250 cm^{-1} [8].

It is interesting to probe the coherent phonon dynamics with a resonant pump beam to generate charged carriers for studying the electron-phonon coupling process. This work is

in progress.

2.4.2 Semiconductor nano crystals

Semiconductor nanocrystals, the so-called quantum dots, provide several novel properties with pre-existing materials. The density of states and bandgap of nanocrystals with typical sizes of 1-10 nm can be tailored for particular applications. These nano sized particles also exhibit enhanced electron-phonon coupling, which is clearly observed in photoluminescence spectrum with persistent vibronic progressions.

There are some reports on the observations of coherent optical phonons in semiconductor QDs, CdSe QDs, InP QDs, *etc.*[9,10] While the high energy optical phonon forms sidebands in optical spectrum, low energy acoustic phonon contributes to excitonic dephasing and homogeneous broadening. Therefore a detailed understanding of the mechanism of generation and damping of confined phonons in QDs is important. QDs prepared with solution-phase chemistry and then embbeded in a polymeric matrix offers a simple while accurate way for QDs sample preparation. We are able to prepare high quality CdSe nanocrystals with narrow size distribution based on a one-pot chemistry developed by Peng [11]. These nanoparticles exhibit fluorescence at about 550-600 nm depending upon the particle size. We plan to over coat CdSe with ZnS to minimize the dangling bonds of CdSe in order to enhance the quantum yield of fluorescence. These core-shell QDs are useful for numerous applications from biomedical fluorescent marker to many other advanced opto-electronic devices. The coherent phonon genration and dynamics of these core-shell QDs are an interesting subject since effects of overcoating layer on the dynamics of confined carriers and confined phonons and their coupling are still unknown.

References of Section II

[1] S. V. Vonsovsky and M. I. Katsnelson, *Quantum Solid-State Physics*, Chap. 2 (Springer-Verlag, Berlin, 1989).

[2] R. Blinc, *Soft Modes in Ferroelectrics and Antiferroelectrics*, (North-Holland, Amsterdam, 1974).

[3] Y. X. Yan, J. Edward, B. Gamble, and K. A. Nelson, *Impulsive Stimulated Scattering,* J. Chem. Phys. 83, 5391 (1985).

[4] Y. X. Yan and K. A. Nelson, *Impulsive Stimulated Scattering II. Comparison to frequency-domain light scattering spectroscopy,* J. Chem. Phys. 87, 6257 (1987).

[5] W. A. Kutt, W. Albrecht, and H. Kurz, IEEE, J. QE28, 2434 (1992); T. K. Cheng, *et al.* Appl. Phys. Lett. 59, 1923 (1991); H. J. Zeiger, *et al.* Phys. Rev. B45, 768 (1992).

[6] R, Merlin, *Solid State Commun.* 102, 207 (1997).

[7] M. Wegner and D. S. Chemla, *Chem. Phys.* 251, 269 (2000).

[8] Phys. Rev. B64, 94301 (2001).

[9] R. W. Schoenlein, *et al.* Phys. Rev. Lett. 70, 1014 (1993).

[10] U. Banin, *et al.*, Phys. Rev. B55, 7059 (1997).

[11] Z. A. Peng and X. Peng, J. Am. Chem. Soc. 124, 2353 (2002); Nano Lett. 1, 333 (2001).

III. Femtosecond Coherent Control Technique

3.1 Pulse Shaping Apparatus

Within the first hundreds femtosecond after ultrafast laser-material interaction, a condensed-phase material does not have enough time to dephase the excitation. Therefore by using a carefully shaped femtosecond laser pulse, it is possible to control the dynamical evolution of a photoexcited system. Indeed this coherent control scheme had been demonstrated on atomic vapor, molecules in solution, and even on a thin film sample. It had been shown that multiphoton-induced fluorescence in an atomic vapor be enhanced with a tailored pulse which is not transform-limited.

To employ coherent control technique for resolving molecular species in condensed phase, a femtosecond pulse shaper based on a liquid crystal spatial light modulator (LC SLM) was designed and constructed [1]. The LC SLM used is 1D array phase modulators with a pitch of 100 μm [2]. Each stripe size is 97 μm with a gap of 3 μm. The schematic of the pulse shaper is depicted in Fig. 3.1.1(a) with the photograph of the real setup presented in Fig. 3.1.1(b).

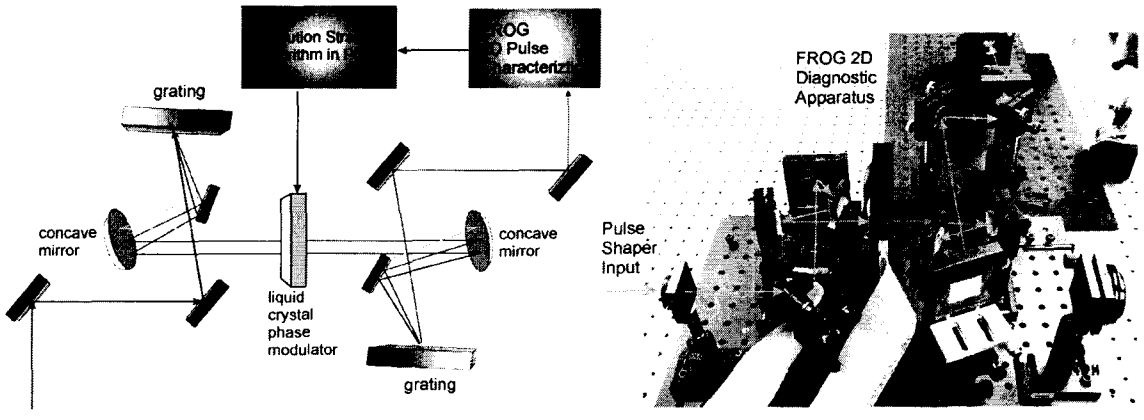

Fig. 3.1.1 (a) Schematic and (b) the photograph of a femtosecond laser pulse shaping apparatus. The setup is based on a 4-*f* dispersion-free apparatus with a liquid crystal phase modulator inserted in the focal plane.

The output of the pulse shaper has been connected to a simple frequency-resolved optical gating (FROG) apparatus for the real-time pulse monitoring [3]. The alignment difficulty

of the pulse shaper can be minimized with the help of the FROG. For the record, the procedure is detailed as follows:

(1) Adjust the input beam to be collimated and propagating a plane parallel to the optical table (*i.e.*, the xz plane).

(2) Align the first grating such that the plane of the grating surface and the rulings of the grating line (along to y-axis) in a plane normal to the optical table. Check that both the specular reflection and the desired first-order diffraction beams propagate in a plane parallel to the table. The optical frequency components spread should also be parallel to the table surface.

(3) Place the first spherical mirror approximately one focal length away from the first grating, with the mirror centered on the first-order diffracted beam. The folding angle should be as small as possible to minimize astigmatism. The height of the mirror should also be adjusted to ensure that the reflected beam still propagates parallel to the table surface. The distance of the mirror from the first grating is not critical.

(4) Position the second spherical mirror two focal lengths away from the first mirror. The mirror should be translated closer to or further from the first mirror until the reflected beam is collimated. The height of the mirror should also be adjusted to ensure that the reflected beam still propagates parallel to the table surface.

(5) The rotation of the second grating about the vertical axis must be set to exactly match that of the first grating. This can be achieved by observing the output beam in the far field and making sure that there is no remaining spatial dispersion (*i.e.*, all the frequency components should be optimally overlapped). To help visualize residual spatial dispersion, one can place a card in the masking plane and sweep it across the spatially dispersed frequencies. If there is residual spatial dispersion at the output, one can see an image of the card sweeping across the output beam; if there is no spatial dispersion,

the output will be uniformly attenuated as the card is moved in the masking plane.

(6) The distance between the second and first grating must be set for exactly four focal lengths in order to obtain zero group velocity dispersion. The grating distance can be fine-tuned by measuring the output pulse duration via intensity cross correlation with an unshaped pulse as a reference. The grating is translated until the output pulse width is minimized. Note that from $\partial^2\phi/\partial\omega^2 = \lambda^3(L-4f)/(2\pi c^2 d^2\cos^2\theta_d)$ the distance deviation from dispersion-free 4*f*-separation causes wavelength-dependent group delay difference (*i.e.*, the frequency dispersion).

(7) Place LC SLM at approximately the back focal plane of the first spherical mirror where individual frequency components are focused to their minimum size. Making sure that the aperture of the SLM is centered on the spatially dispersed frequency spectrum. Monitoring the output spectrum from the pulse shaper to observe the features placed by the mask onto the spectrum

3.2 Pulse Shaping with Gerchberg-Saxton Algorithm

Pulse shaping is usually based on linear filtering of the pulses in the Fourier domain. Thus as the pulse shaper is aligned and ready to use, the first step to generate a specific user-defined pulse shape is the preparation of a driving voltage pattern for the LC SLM. To shape a given pulse to an arbitrary temporal waveform both the spectral amplitude and the phase have to be modified. A pulse shaper must provide the necessary complex spectral transfer function

$$T(\omega) = E_{out}(\omega)/E_{in}(\omega) \qquad 3.2.1$$

which transforms a given input pulse represented by its spectral electric field $E_{in}(\omega)$ to a specific tailored output pulse $E_{out}(\omega)$. Modulators, which only change the phase of the spectral components, can conserve the pulse energy.

$$E_{out}(\omega) = E_{in}(\omega) e^{i\Delta(\omega)} . \qquad 3.2.2$$

Although phase-only pulse shapers can be used to yield a large variety of possible output waveforms, there exists no unique way to calculate the phase modulation that is needed for the generation of a specific pulse. However, phase-only shapers are still preferred if only the temporal intensity profile is of importance not the phase.

In this research we investigate two algorithms to be used for the driving pattern determination. The first method, the Gerchberg-Saxton algorithm [4], is borrowed from the image analysis community, which had been widely employed to determine phases from image. The application of Gerchberg-Saxton algorithm on phase-only pulse shapers is detailed in Fig. 3.2.2. [5]

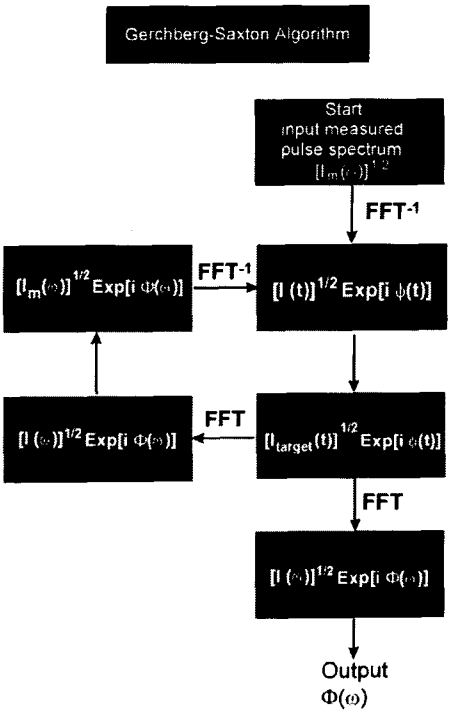

Fig. 3.2.1 Flow chart of the Gerchberg-Saxton algorithm used to deduce the phase modulation pattern of a phase-only pulse shaper [5]

To initialize the algorithm the amplitude of the input field is chosen to be the square root of the measured input pulse spectrum $\sqrt{I_m(\omega)}$. The unknown spectral phase is replaced

with a random phase pattern to avoid any potential bias. The spectral field is transformed to the time-domain by an inverse Fourier transformation and the resulting temporal amplitude $\sqrt{I(t)}$ is replaced by the target amplitude $\sqrt{I_{\text{target}}(t)}$. The temporal phase φ(t) remains unchanged (the algorithm restrains only the temporal amplitude of the pulse not the phase). Next, the Fourier transformation of the pulse back to the spectral domain is performed. Since the temporal profile has been altered, a modified spectral phase Φ(ω) is obtained. The spectral amplitude is then replaced with the spectral amplitude of the input pulse $\sqrt{I_m(\omega)}$. The phase remains unchanged and the next iteration reconvenes. The iteration stops when the process stagnates at a certain level. The phase Φ(ω) constitutes the desired phase modulation which transforms the input pulse as close as possible to the target pulse when it is applied on the LC-SLM. This algorithm can be viewed as a deterministic method and it delivers results much faster than other optimization schemes based on try-and-error process.

The algorithm had been coded into a Fortran 90 program. The apparatus was used to convert a 30-*fs* femtosecond pulse with a central wavelength of 800 nm into a variety of target profiles. The target pulse profile contains three pulses with characteristics shown as follows: $E(t)=0.7\ E_0(t+200\ fs)+E_0(t)+0.7\ E_0(t-200\ fs)$. The resulting FROG pattern of the shaped pulse and the corresponding target pulse are presented in Fig. 3.2.2, with the horizontal axis showing the optical frequency and the vertical axis showing the time.

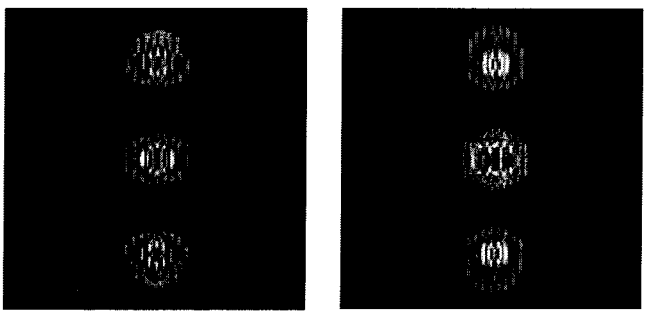

FROG Pattern of the Target Pulse Profile

FROG Pattern of the Shaped Pulse Profile

Fig. 3.2.2 FROG patterns of (LH) the target and (RH) the shaped pulse. The target pulse profile constitutes

of three pulses with relative amplitudes of 0.7, 1.0, 0.7 and locating at –200, 0, and 200 *fs*, respectively.

As it can be seen the shaped pulse agrees very well with the target profile from the spectral modulation to temporal profile. Judging from the fact that only the spectral phase being modulated, the quality of the design with Gerchberg-Saxton algorithm is quite satisfactory. This methodology is suited for the femtosecond pulse design, at least for the primitive search purpose at the beginning of search cycle.

3.3 Pulse Shaping with Evolution Algorithm

Evolution strategy (ES) is a global optimization procedure that belongs to the larger group of evolutionary algorithm (EA) [6]. There exist two representatives of EA: ES and genetic algorithm (GA). One of the most important differences lies in the representation of a possible solution to a given problem. This representation uses real numbers in ES, while a string of binary numbers is used in GA. Moreover, in ES some of the optimization parameters are self-adaptively adjusted during the optimization procedure. This self-adaptiveness as well as the real representation makes the implementation of ES more straightforward than the implementation of GA.

In terms of ES [7], the parameters that are changed by the algorithm are called genes and a combination of the total number N of genes is referred to as an individual. In ES, each gene is comprised of object variables and strategy variables. For the pulse shaping purpose, the object variables can be the phase retardance on LC-SLM, and the strategy variables control the mutation step lengths of the object variables in each cycle. ES algorithm then works simultaneously on a number of individuals called population. A new population replaces an old one by using the genetic operations of recombination, mutation, and selection. The individuals are evaluated to select the fittest individuals.

We had employed the ES algorithm for shaping femtosecond pulses. The flow chart

of the application is depicted in Fig. 3.3.1. First a sufficiently large population of 100 individuals are generated randomly. The 15 fittest individuals are selected and used to build the population of the next generation. The ratio 100/15~7 is chosen to guarantee a sufficiently low selection pressure. We found such a parameter combination is good enough to yield a rapidly convergence. In fact, the apparatus had demonstrated a capability to reshape a highly distorted pulse into the transform-limited form within 90 generations (see Fig. 3.3.2)

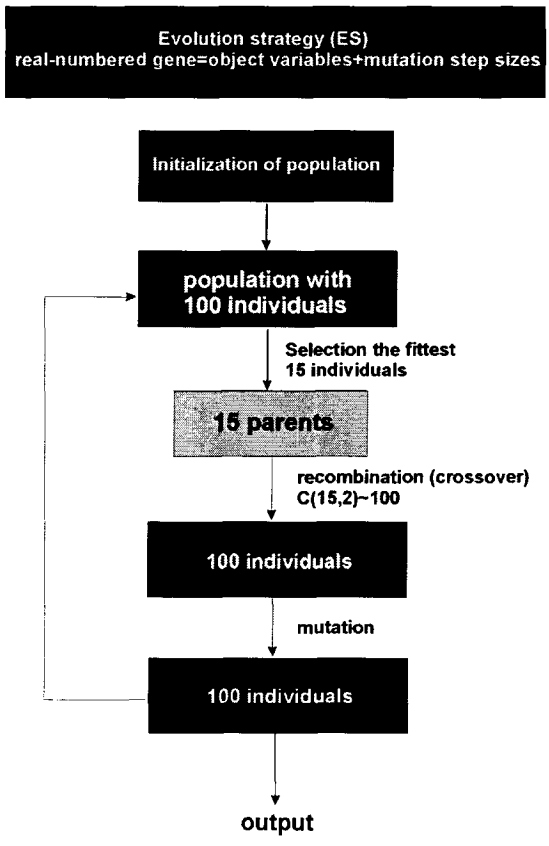

Fig. 3.3.1 Flow chart of the ES algorithm used for pulse shaping with a 4*f*/dispersion-free pulse shaper apparatus.

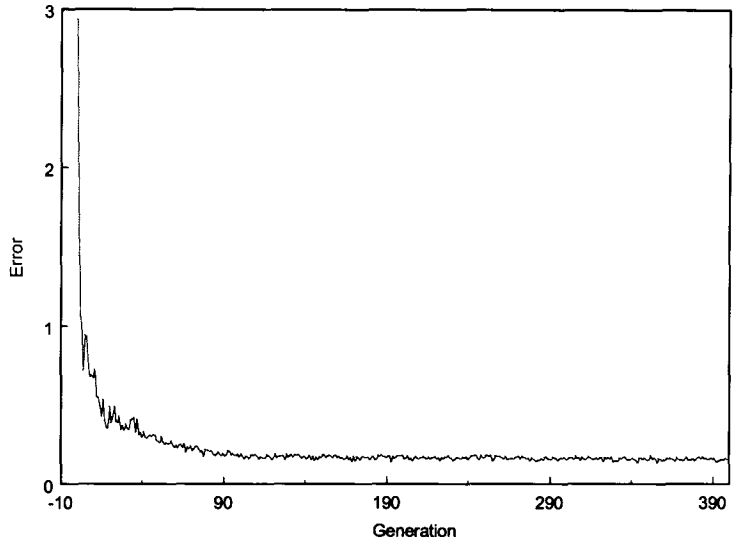

Fig. 3.3.2 Error between the shaped pulse and the transform-limited pulse as plotted for each ES generation.

3.4 Adaptive Pulse Shaping

To show that the phase-only pulse shaper apparatus with ES algorithm can reliably remove the accumulated phase distortion and concerts the distorted pulse into transform-limited profile, we sent a ultrafast laser pulse at 800 nm with 30-*fs* FWHM duration through a 2-mm thick color glass filter. The color glass filter generates a significantly nonlinear phase shift with the FROG pattern of the resulting phase distorted pulse shown in Fig. 3.4.1 (LH). The ES algorithm operates on 100 individuals with 15 parents. Two genetic operations of random arithmetic crossover and dynamic mutation are employed. The results are presented in Fig. 3.4.1.

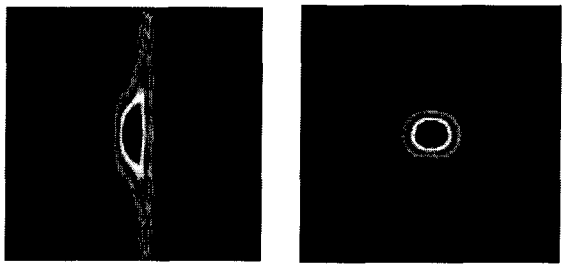

FROG Pattern of Distorted Pulse

FROG Pattern of Shaped Pulse

Fig. 3.4.1 FROG patterns of (LH) the phase distorted pulse and (RH) the shaped output from a phase-only pulse shaper with ES algorithm.

The adaptive ability of a pulse shaper may prove to be useful for many applications [8]. Here we suggest one of the these potential applications. The shaper output can be brought to excite a moelcular object in a specific environment and a merit function is defined to train the ES algorithm. After a suitable pulse profile is found, the shaped output can be scanned on a sample to discover the distribution of the moelcule in the specific environment. A chromophore embedded inside an inhomogeneous matrix is one typical example.

References of Section III

[1] A. M. Weiner, Rev. Sci. Instrum. 71, 1929 (2000).

[2] A. M. Weiner, *et al.* IEEE, J. Quantum Electron. QE28, 908 (1992).

[3] D. J. Kane and R. Trebino, IEEE, J. Quantum Electron. QE29, 571 (1993).

[4] R. Gerchberg and W. O. Saxton, Optik 35, 237 (1971).

[5] M. Hacker, G. Strobrawa, and T. Feurer, Optics Express 9, 191 (2001).

[6] T. Back, *Evolutionary Algorithm in Theory and Practice* (Oxford Univ. Press, New York, 1996).

[7] D. E. Goldberg, *Genetic Algorithms in Search, Optimization, and Machine Learning* (Addison-Wesley, Reading, 1993).

[8] A. Assion, *et al.*, *Control of Chemical Reaction by Feedback-Optimized Phase-Shaped fs Laser Pulses*, Science 282, 919 (1998); R. Bartels, *Shaped-Pulse Optimization of Coherent Emission of High-Harmonic Soft X-Rays*, Nature (London) 406, 164 (2000); T. C. Weinacht, *et al.*, *Controlling the Shap of a Quantum Wavefunction*, Nature (London) 397, 233 (1999).

IV. Complete Optical Field Characterization of Extremely Weak Femtosecond Optical Signal

In the past decade, various ultrafast pulse analyzing methodologies [1] have been developed. Frequency-resolved-optical-gating (FROG) [2], developed by the Trebino's group, represents a typical example of characterizing a ultrafast optical signal. FROG and other related techniques are based on nonlinear optical processes, therefore fairly high optical intensity is required. Currently, the most sensitive FROG technique requires at least a few pico-joules with multi-shot detection [3] and about 100 nano-joules for a single shot measurement. The need for fairly high intensity has severely limited their applications. For example, the techniques are not suitable for the complete characterization of weak luminescence. Therefore, an important issue in the ultrafast optical diagnosis is the development of a highly sensitive technique for measuring extremely weak signal from molecules of interest in biology, chemistry and optoelectronics.

In this research, we developed a technique to allow time-resolved spectral measurements of ultraweak optical signal at atto-Joules level (10^{-18} J) in single shot. The time-resolution achieved is mainly limited by the pulse duration of the pump laser. The technique employs optical parametric amplification (OPA) to achieve the few-photon detection sensitivity. The gain of OPA can be as high as 10^9 to 10^{10} [4], depending on the pumping intensity, the nonlinear medium used, and the intensity of the signal. By combining OPA with FROG technique, a complete characterization of an optical signal (magnitude and phase) with few-photons sensitivity could be achieved.

The basic idea of this technique is to use a short laser pulse to excite a sample. An OPA device, which is synchronously pumped by a strong laser pulse, amplifies the resulting weak signal from the photoexcited sample. The amplified signal can be analyzed with a

spectrograph versus different delay times, which allows complete field diagnosis of an optical signal in a single shot fashion. An typical setup is shown in Fig. 4.1.

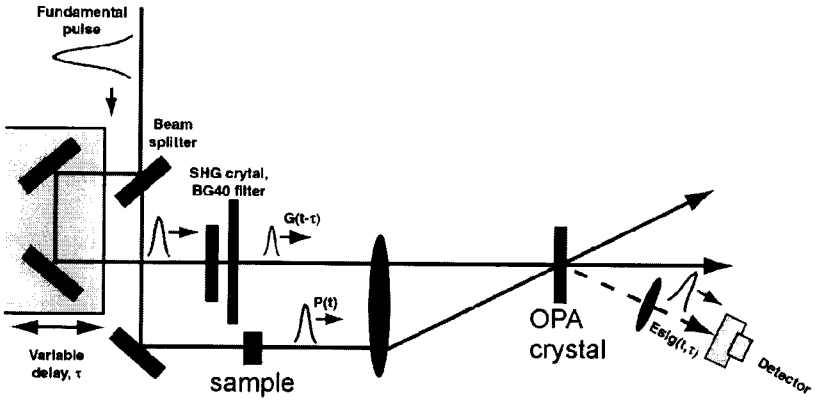

Fig. 4.1 Optical configuration for ultra-sensitive OPA-FROG apparatus with gain.

The unique features of the OPA-FROG are gain and applicability to long-wavelength signals. To demonstrate these advantages, the infrared output at 1.9 μm taken from an optical parametric amplification system pumped by a femtosecond $Ti^{3+}:Al_2O_3$ regenerative amplifier was used to simulate the long wavelength signal generated by a sample. The infrared beam (the idler wave) was seeded into a 2-mm long BBO OPA crystal pumped at 412-nm from the second-harmonic of the femtosecond $Ti^{3+}:Al_2O_3$ laser beam [5]. The amplified signal wave at 526 nm was analyzed with a spectrograph at different delay time. The results are presented in Fig. 4.2, where the intensity (solid line) and the phase (dashed line) of the spectrum (LH) and the temporal profile (RH) deduced from the measured FROG patterns of the amplified signal wave (RH) are shown. The quality of FROG pattern is improved with OPA amplification than that without the amplification (LH), and leads to much smaller FROG fitting error (0.023).

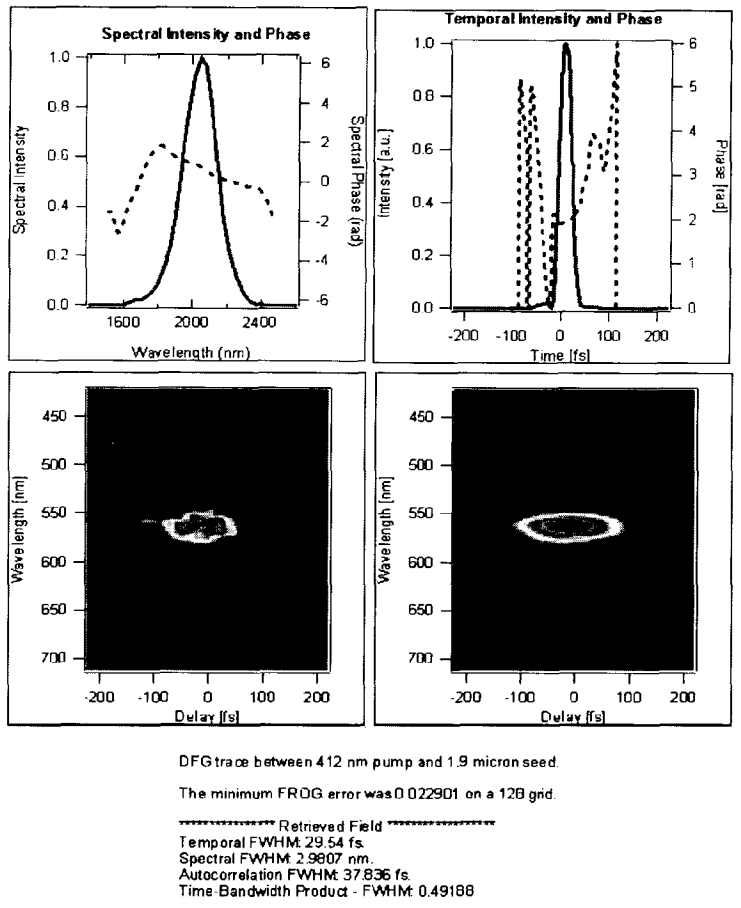

Fig. 4.2 The intensity (solid line) and the phase (dashed line) of the spectrum (LH) and the temporal profile (RH) deduced from the measured FROG pattern (RH). The FROG pattern without OPA amplification (LH) is also included for comparison.

To show the minimum detectivity of the OPA-FROG apparatus, we use a seed pulse at 532 nm into the OPA crystal with a variety of attenuation and analyzes the resulting amplified FROG pattern. We found a satisfactory pattern can still be obtained when a seed pulse with an energy as small as 10 atto Joules being used. At such a low energy level, each pulse contains about 30 photons only. Therefore we confirm that few-photon detection sensitivity can indeed be achieved with OPA-FROG. The resulting pattern is shown in Fig. 4.3.

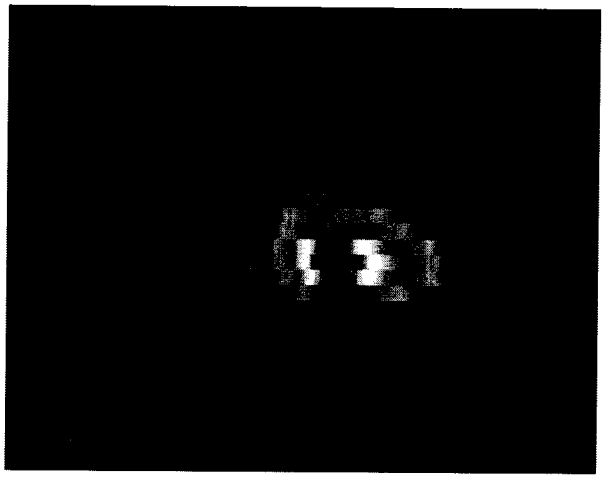

Fig. 4.3 The OPA-FROG pattern for a extremely weak optical pulse at 532 nm with a pulse energy about 10 atto Joule. The horizontal direction indicates the spectral axis and the vertical axis is the delay time.

To employ OPA-FROG for probing non repetitive events, single-shot detection is indispensable [6]. We redesign OPA-FROG to reflect this technological development trend. The new design is shown in Fig. 4.4.

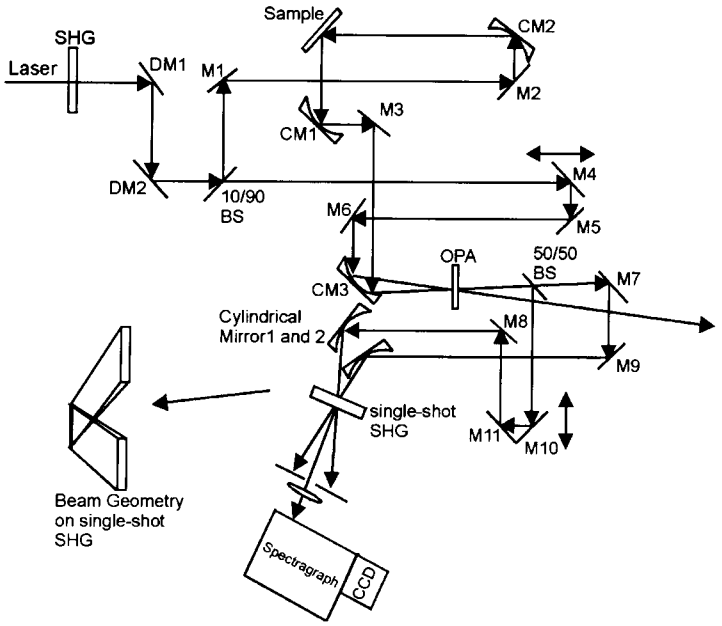

Fig. 4.4 Optical configuration for ultr-sensitive single-shot FROG measurement

In brief, a laser beam from a regeneratively amplified Ti: sapphire laser is frequency-doubled with an 1-mm long BBO crystal to produce SHG at 400 nm. The laser

beam is then split into two parts with a beam splitter (10R/90T). 10% of the beam is used to pump a sample to generate fluorescence. We use a concave mirror CM1 to collect the fluorescence from sample and then collimate it into the OPA for further amplification. The majority of the beam is used to pump an OPA. The pumping intensity of OPA is about 100 GW/cm^2. The sample fluorescence can be amplified in the OPA with a gain of 10^8-10^{10} without significant distortion. The preliminary data show that as long as the signal intensity is less than 1 pJ, no gain saturation was observed in the OPA. Therefore the spectral and temporal distortion of the amplified signal is insignificant.

The amplified signal beam is then split into two parts by a 50/50 beam splitter (50/50 BS). Each amplified beam is then focused by a cylindrical mirror in the horizontal direction and it forms a vertical line at the focal plane of the cylindrical mirror. Two focused beams are then directed onto a SHG crystal with a small angle (5-10 degrees) in the vertical plane. After a suitable delay, two beams overlap in the crystal and generate SHG in the forward direction. Since the SHG yields cross-correlation of two input beams, the intensity distribution of SHG in the vertical direction provides the information about the pulse profile of the amplified beam. The SHG beam generated in the forward direction of the crystal is focused by a cylindrical lens onto the entrance slit of a CCD-spectrometer. The beam is dispersed by the spectrometer in the horizontal direction while the distribution in the vertical direction remains unchanged. The output of the spectrometer forms a 2-D pattern on the 2D-CCD detector with the horizontal direction being the spectral distribution, and the vertical direction giving the pulse profile of the signal.

In this design, there is no moving parts in the delay time, the complete field information of an optical signal can be obtained in a single shot. [23]

The advantages of this proposed single-shot OPA-FROG are significant in the following aspects:

First, the scheme doesn't need to scan the delay-time to obtain the pulse shape information. This is particularly important for the case that photoexcited sample may be degraded with laser exposure so that the spectral properties of the sample change with time. The development of a single-shot OPA-FROG apparatus would make the measurement of ultrafast and ultraweak fluorescence becomes practical.

Secondly, this scheme is highly suited for the case when the signal is fluctuates from pulse to pulse. By using this design, one can obtain all the information in a single shot as long as the amplified signal is strong enough with an appreciable OPA gain. Even if the signal to be measured is not strong enough with a single shot measurement, one can use multi-exposure of single shot to accumulate signal. For a kHz regen-amplifier laser system, multi-exposure of single shot takes very little extra time (less than 0.1 s) to acquire the signal needed.

Thirdly, the proposed technique possesses an extremely high sensitivity. Our estimation indicates that one could perform FROG pattern measurements versus time with sensitivity at atto-Joules level. This is probably the highest sensitivity one can imagine at present.

Finally, the proposed technique allows FROG measurement of light signal to be extended from the visible to the infrared [7]. For example, with a type-I BBO crystal, the longest wavelength that one can reach is about 2.2-2.3 μm. Such a limit can be extended to 3-4 μm by using other nonlinear crystals, such as $KNbO_3$. It is known that it is very difficult to measure weak infrared emission sensitively due to lack of sensitive IR detector. In the case of OPA, the idler beam and the signal beam are generated in pair and highly correlated to each other. For a 400-nm pumped OPA, the signal wave lies in a range from 440 nm to the degenerate point at 800-nm, while the idler wave ranges from 800-nm to the near IR or mid-IR depending on the crystal used. When an infrared signal is sent to an

OPA, it is amplified as the idler beam and at the same time a signal wave is created at the difference frequency of the pump and the idler. Therefore, one can probe the idler wave in the infrared by examing the amplified signal wave, which generally lies in the visible or near infrared and the photons yielded can be detected sensitively.

References of Section IV

[1] See for example in IEEE, J. Sel. Topics Quantum Electron. 4, (1998)

[2] D. J. Kane and R. Trebino, IEEE, J. Quantum Electron. QE29, 571 (1993).

[3] Rick Trebino, "Frequency-Resolved Optical Gating: The measurement of Ultrashort Laser Pulses" (Kluwer Academic Publisher, 2002)

[4] See special issues on OPA and OPG in J. Opt. Soc. Am. B10, No. 9 and No. 11 (1993); J. Opt. Soc. Am. B 12, No. 11 (1995).

[5] S. R. Greenfield and M. R. Wasielewski, "Optical Parametric amplification of femtosecond pulses tunable from the blue to the infrared with microjoules energies", Appl. Opt. 34, 2688-2691 (1995); V. Petrov, F. Seifer, and F. Noack, "Visible optical parametric generator producing nearly bandwidth-limited femtosecond light pulses at 1-KHz repetition rate", Appl. Opt. 33, 6988-6991 (1994); H. Wang, K. S. Wong, D. Deng, Z. Xu, K. Wong and J. Y. Zhang, "Kilohertz femtosecond UV-pumped visible B-barium borate and lithium triborate optical parametric generator and amplifier", Appl. Opt. 36, 1889-1893 (1997).

[6] D. J. Kane and R. Tribino, "Single-shot measurement of the intensity and phase of an arbitrary ultrashort pulse by using frequency-resolved optical gating", Opt. Lett. 18, 823-825 (1993).

[7] See for example, D. T. Reid, *et al.*, *Amplitude and phase measurement of mid-IR femtosecond pulses by using cross-correlation frequency-resolved optical gating*, Opt. Lett. 25, 1478 (2000).

V. Conclusions and future prospect

In this research, we have successfully developed and established some highly useful ultrafast linear and nonlinear optical techniques for probing the dynamics of condensed-phase materials. The differential reflectivity/transmission apparatus offers unique opportunity to study the lattice dynamics of crystalline samples in bulk or in dimensional confinement systems. Ultrafast pulse shaping technique based on a $4f$ dispersion free apparatus is developed to provide the capability to control ultrafast laser material interaction. We implement Gerchberg-Saxton algorithm in a phase-only femtosecond pulse shaper for an efficient and accurate pulse design. Based on the FROG pattern analysis, we show that this method can be used to generate an ultrafast pulse train with a user-specific profile for coherent control experiment. This is highly useful for the study of coherent phonon dynamics in advanced materials for novel applications.

For the control on more complicated ultrafast laser material interaction, an adaptive pulse shaper may be the correct approach. To allow the investigation into such research topics, we implement evolution strategy algorithm into the femtosecond laser pulse shaping apparatus with a LC-SLM phase modulating device. We show that in 90 generations, the apparatus can compensate the phase distortion of a distorted pulse and bring it back to transform-limited profile. This apparatus is therefore useful for mapping a specific molecule in an inhomogeneous environment by properly training the adaptive feedback loop.

The applicability of nonlinear optical methodology is often limited owing to its low signal strength. A second-harmonic autocorrelator is usually implemented in a FROG-based ultrafast laser diagnostic system. This becomes problematic in use of FROG technique for an experimental detection. We develop an OPA-FROG to solve this

difficulty. OPA is used to provide an appreciable gain for a weak optical input signal and therefore FROG pattern analysis can reliably proceed. We show the OPA-FROG can achieve a detection limit as low as 10 atto Joule, which corresponds to 30 photons in single pulse. An extension to single-shot version of the OPA-FROG is proposed for the future study.

These advanced coherent optical techniques established in this research provide a solid platform and unique opportunity for the future study on the dynamical evolution and coherent control of ultrafast laser material interactions in bulk and in dimensional confined systems. Preliminary studies on coherent phonon dynamics in ZnSe film and in quantum dot systems have yielded informative results. Continued investigation into second phase along this direction is currently undergoing. Particularly attention will be paid to the dynamics of spin and electron transport across various interfacial systems, which may turn out to be an important issue for spintronic device physics.

LIQUID CRYSTALS, 2002, VOL. 29, NO. 10, 1283–1290

Taylor & Francis
Taylor & Francis Group

Molecular alignment and field-induced reorientation in a twisted nematic liquid crystal pi-cell

WEN-TSE SHIH and JUNG Y. HUANG*
Institute of Electro-Optical Engineering, Chiao Tung University, Hsinchu, Taiwan, ROC

(*Received 14 January 2002; in final form 15 April 2002; accepted 22 April 2002*)

A twisted nematic pi-cell has been studied by optical transmission measurement, polarized Fourier-transform infrared (pFTIR) absorption spectroscopy, and Raman spectroscopy. Our pFTIR results suggest that the LC molecules undergo a restricted rotation about the molecular long axis. The rise and decay times of the optical response were found to be 6 ms and 1.6 ms, respectively. The switching dynamics of the twisted pi-cell was also studied using time-resolved Raman spectroscopy. A normal mode associated with the C–H out-of-plane wag on the LC core was found to be enhanced after the electric field was switched off. Our data show that LC molecules in the twisted pi-cell do not rotate like a rigid molecule during the field-induced reorientation process. The methods employed in this study have yielded valuable information about LC alignment and field-induced reorientation with respect to functional group specificity.

1. Introduction

Twisted-nematic (TN) liquid crystal cells have been widely used in active matrix liquid crystal display (AMLCD) technology. Unfortunately in the TN mode, slow response and angular dependence of the image quality degrade the device performance. To overcome these drawbacks, the pi-cell [1] or optical compensated birefringence (OCB) LCD [2] have been proposed. However, the bend configuration in both pi-cell and OCB device is unstable at low driving field. In these devices, a more stable splay configuration appears first [3], and a long warm-up period is needed to transform the LC device from the splay state to the bend state. This becomes problematic in multiplexed display applications, where the conversion of the inter-pixel LC molecules from the splay to the bend configuration is accompanied by disclination generation [1, 3]. The display quality is thereby degraded. Two methods have been proposed for solving the problem. The first is to add a small fraction of polymeric chains into LC films to stabilize the bend configuration. Unfortunately, this approach produces hysteresis in the optical transmittance and decreases the optical quality, with light scattering from the index mismatch between the liquid crystal and polymer. The second method adopts a high pretilt angle in the LC film. Although the stability of the bend configuration indeed improves with high pretilt angle, the device response time increases.

*Author for correspondence; e-mail: jyhuang@cc.nctu.edu.tw

In this paper, a twisted nematic LC pi-cell doped with chiral molecules is described. The LC cell exhibits a stable bend configuration. Although the switching process in a twisted pi-cell has been investigated by optical transmission measurement and theoretical simulation [4], the molecular alignment with varying field strength has not yet been explored experimentally. In this regard, vibrational spectroscopy is better suited for probing the molecular orientation than absorption spectroscopy, owing to its 'fingerprinting' capability. In this paper, we report the results of molecular alignment and re-orientation in a twisted pi-cell with polarized Fourier-transform infrared absorption (pFTIR) spectroscopy [5] and Raman spectroscopy [6].

2. Experimental

Samples of twisted pi-cell were assembled with two ITO-coated CaF_2 plates. The substrates were coated with a $700 \sim 800$ Å thick RN1842 (from Nissan Co.) alignment layer and rubbed to yield a 2° pretilt angle for the LC molecules used. The cell gap was maintained at $d = 6\,\mu m$ with proper spacers. ZLI 2293 liquid crystal (from Merck Co.), doped with 0.71 wt % S-811 left-handed chiral molecules, was used to fill the empty cell above the LC clearing temperature. The cell was then slowly cooled to 30°C to produce a pitch of $p = 15\,\mu m$ and satisfy the condition $d/p = 0.4$ [3]. The LC cells were then enclosed with UV-cured sealant.

We first investigated the optical transmittance (T) versus voltage (V) by inserting the LC cell into a crossed

Liquid Crystals ISSN 0267-8292 print ISSN 1366-5855 online © 2002 Taylor & Francis Ltd
http://www.tandf.co.uk/journals
DOI: 10.1080/02678290210160097

polarizer-analyser set-up with a helium-neon laser at 6328 Å as the light source. The rubbing direction of the cell substrates was rotated 45° from the transmission axis of the input polarizer. An electric field with voltage increasing from 0 to 10 V was first applied on the LC cell. The transmittances obtained are presented in figure 1 (filled squares). The LC cell was then stabilized at the high field for a brief period and then the voltage was decreased from 10 to 0 V. The resulting transmittances are shown with the open symbols. No hysteresis was observed, indicating that the underlying LC configuration is stable. To explore further, we performed a simulation on the LC cell with the elastic theory of continuum medium under varying voltage. The calculated optical transmission shown by the solid curve agrees reasonably well with experimental observation, indicating that the calculated LC profiles (presented in the inset at 0, 2, 4 and 10 V) are precise in depicting the LC configuration.

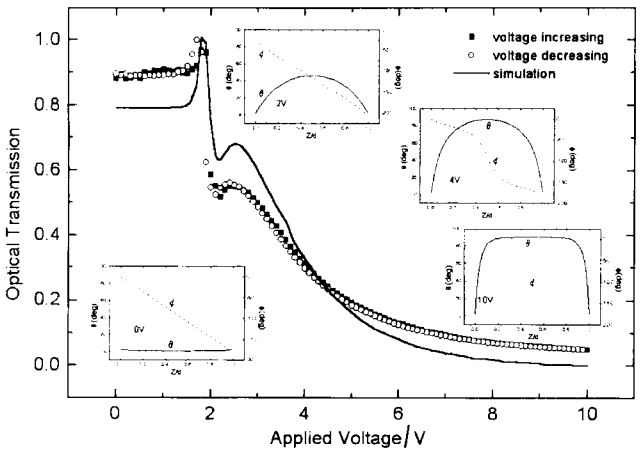

Figure 1. Measured optical transmission of a twisted pi-cell as a function of applied voltage. The calculated T–V curve (solid curve) and the underlying director profiles (inset) at 0, 2, 4, and 10 V are included for comparison.

FTIR spectra from 900 to 4000 cm^{-1} with 4 cm^{-1} resolution were recorded with an Oriel MIR-8000 FTIR spectrometer equipped with a liquid nitrogen cooled MCT detector. A wire grid polarizer on a rotation stage was used to control the polarization of the incident IR beam. The sample was excited with a 2 kHz bipolar square-wave with varying voltage.

An experimental set-up used to acquire transient Raman spectra from a LC cell during field-induced switching is depicted in figure 2. The incident laser beam with a wavelength of 523 nm was polarized along the rubbing direction of the pi-cell. The timing between the laser probing and the electrical driving field on the LC cell was controlled with a combination of functional generator and digital delay generator. The Raman scattered photons were collected by a microscope objective lens and detected with a charge coupled device (CCD) camera through a spectrograph. The CCD was cooled to −20 °C with a thermoelectric cooler.

3. Results and discussion

3.1. *Polarized Fourier-transform infrared absorption spectroscopy of a twisted LC pi-cell*

A typical FTIR spectrum of a twisted LC pi-cell is presented in figure 3. The polarization of the incident infrared beam is oriented to the rubbing direction. The

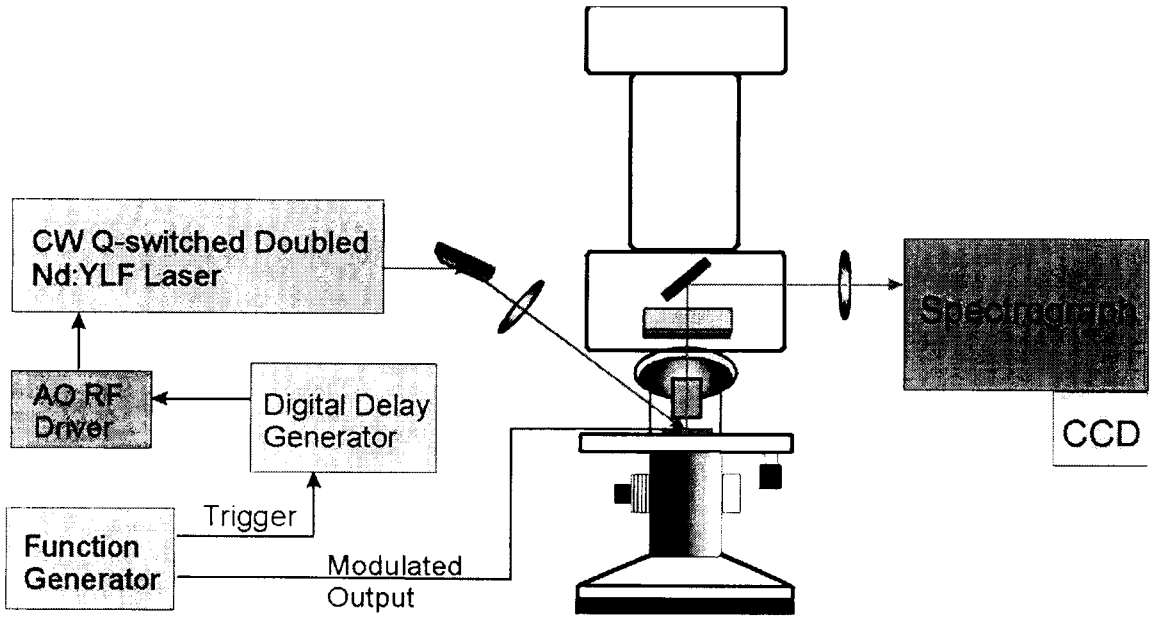

Figure 2. Experimental set-up for acquiring transient Raman spectra from a LC cell during the field-induced switching process.

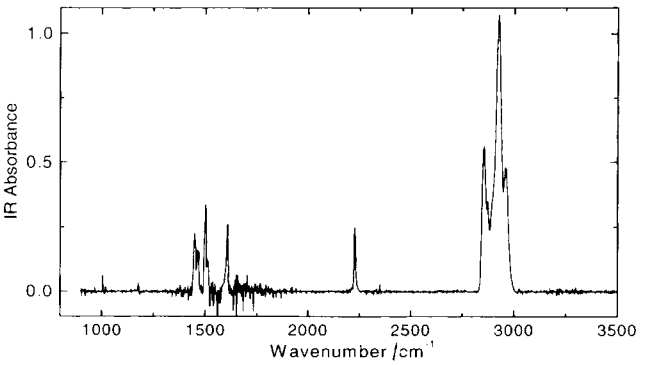

Figure 3. Fourier-transform infrared absorption spectrum of a twisted pi-cell with an applied voltage of 0 V. The polarization of the incident infrared beam is oriented to the rubbing direction.

six peaks were found to lie at 1448, 1502, 1606, 2228, 2851, and 2924 cm^{-1}. The highest two peaks at 2851 and 2924 cm^{-1} are contributed from the symmetric (s-CH_2) and anti-symmetric (a-CH_2) CH_2 stretches along the alkyl chain of the LC molecules. The peak at 2228 cm^{-1} can be attributed to C≡N stretch and the features at 1606 and 1502 cm^{-1} are mainly from the C=C stretch of the LC core. A combination of the C–C stretch and the C–H in-plane wag on the LC core leads to the 1448 cm^{-1}-peak. The mode assignments are summarized in the table, accompanied by the calculated normal-mode vibrations of the cyanobiphenyl core using a density functional theory package [7].

In figure 4 the measured IR peak intensities are presented as a function of the azimuthal angle between the infrared polarization and the rubbing direction of the cell. The three major peaks from the LC core at 1502, 1606 and 2228 cm^{-1} exhibit very similar azimuthal patterns. Their peak amplitudes and dichroic ratios also display significant dependence on the applied voltage.

To investigate the molecular alignment further, we performed simulations with various LC alignment

Table. Calculated and measured normal-mode frequencies of cyano biphenyl.

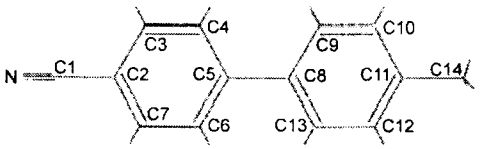

Normal modes	Vibration frequency/cm^{-1}	IR absorption (calc.)	Symmetry
1. C=H stretch			
s-CH_2	2851 (IR) 2851 (Raman)		
a-CH_2	2924 (IR)		
f-CH_3	2937 (Raman)		
2. C_1≡N stretch	2237 (calc.)	89.8	A_1
	2228 (IR) 2228 (Raman)		
3. Biphenyl C=C stretch	1605 (calc.)	46.3	A_1
	1606 (IR) 1606 (Raman)		
	1502 (IR)		
4. (a) biphenyl C–C + C–H in-plane wag	1446 (calc.)	29.5	A_1
	1448 (IR)		
(b) C_5–C_8 stretch + C–H in-plane wag	1261 (calc.)	6.5	A_1
	1265 (Raman)		
	1240 (Raman)		
5. C(biphenyl)–H in-plane wag	1095 (calc.)	13.9	A_1
	1177 (Raman)		
6. Biphenyl in-plane angular distortion	985 (calc.)	4.2	A_1
	957 (Raman)		
	510 (calc.)	5.9	
7. C–H out-of-plane wag	507 (calc.)	9.9	B_1
	544 (calc.)	6.3	
	664 (calc.)	42.8	
	713 (calc.) 705 (Raman)	11.8	
	742 (calc.)	45.7	
	818 (calc.) 790 (Raman)	23.2	
	821 (Raman)		

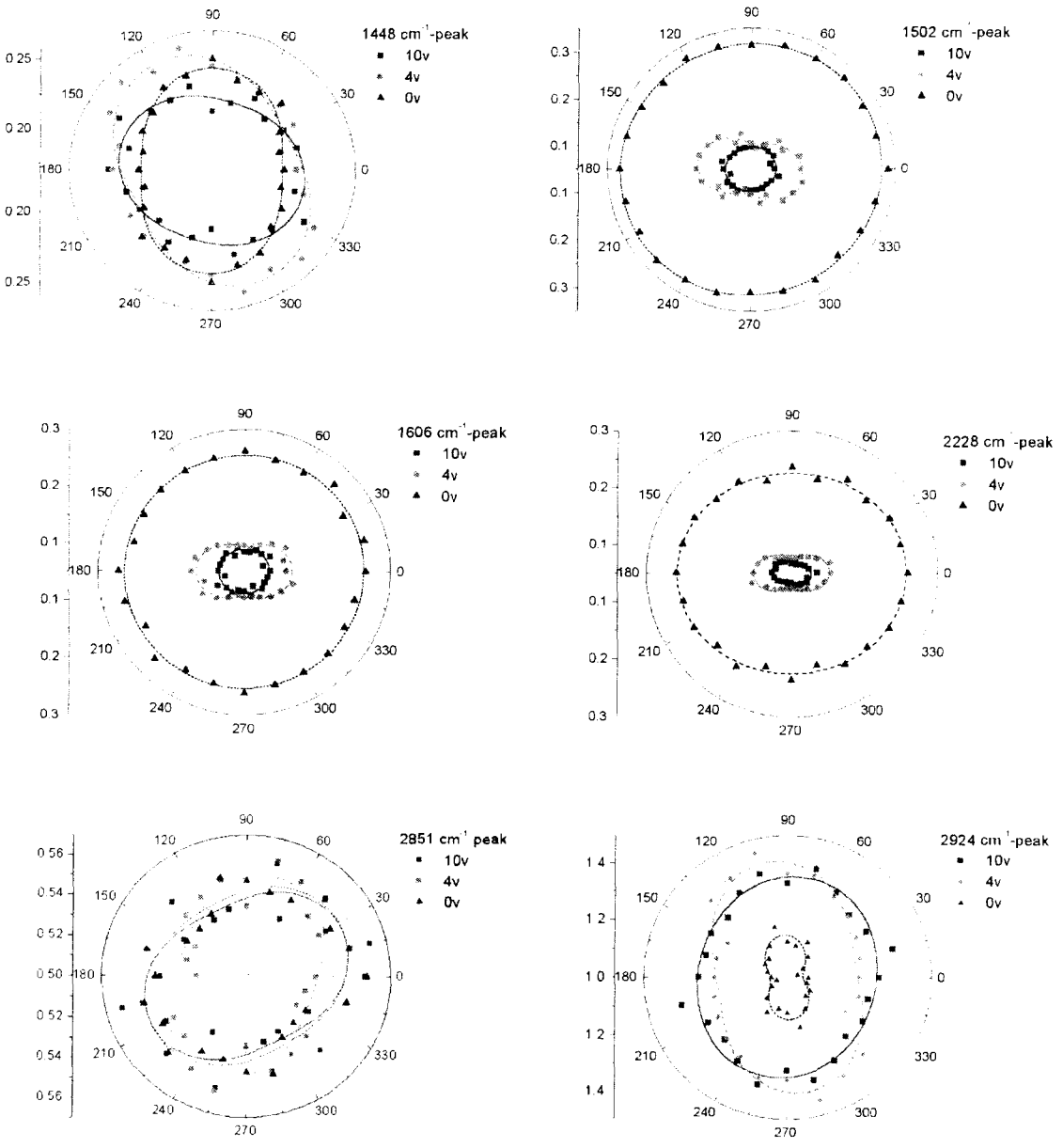

Figure 4. Azimuthal patterns of the infrared absorption peaks of a twisted pi-cell with varying applied voltages. The azimuthal angle denotes the angle between the infrared polarization and the rubbing direction of the cell.

models. Note that the infrared absorption by an optical anisotropic film can be properly described with a 2nd rank absorbance tensor [8]

$$A(\Phi) = \frac{N\pi}{3c} \int [\mu_g^{(K)} \cdot \hat{E}]^2 f(\Omega)\, d\Omega \qquad (1)$$

where Φ denotes the angle between the incident infrared polarization and the X-axis of the laboratory coordinates system (see figure 6), and $f(\Omega)$ is the orientational distribution of the dipole moment derivative. With a normal incidence on the XY-plane, the integrated IR absorbance can be expressed as

$$A(\Phi) = \frac{1}{3}A - \frac{1}{2}\sqrt{\frac{2}{3}}W_1^{lab} + \sqrt{2}\,W_2^{lab}\cos 2\Phi. \qquad (2)$$

Here the anisotropic absorbance tensor W_i^{lab} can be related to the square of the molecular dipole derivatives W_i^{mol} by [8]

$$W_1^{lab} = \sqrt{3/2}\,a_Z = W_1^{mol}\langle S_{11}\rangle + W_2^{mol}\langle S_{21}\rangle$$
$$W_2^{lab} = \sqrt{1/2}(a_X - a_Y) = W_1^{mol}\langle S_{12}\rangle + W_2^{mol}\langle S_{22}\rangle \qquad (3)$$

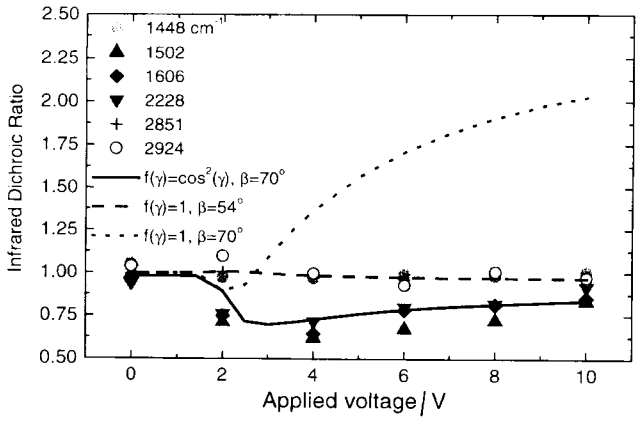

(a)

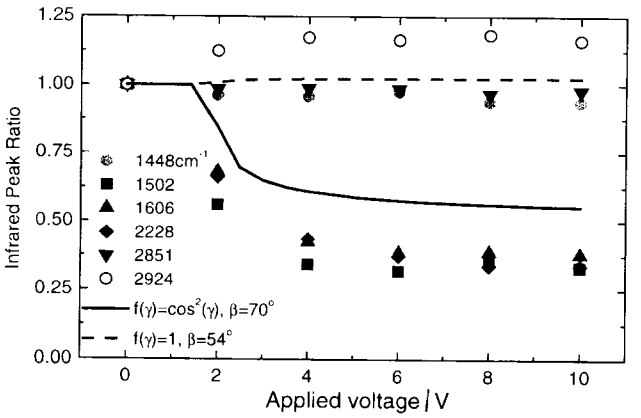

(b)

Figure 5. The infrared dichroic ratio (*a*) and the intensity ratio (*b*) of the infrared absorption peaks plotted as a function of voltage. Simulated curves with various orientational distributions of LC molecules are included for comparison.

with

$$W_1^{\mathrm{mol}} = \sqrt{3/2}\,(\mu_{g,\xi}^{(K)})^2$$
$$W_2^{\mathrm{mol}} = \sqrt{1/2}\,[(\mu_{g,\eta}^{(K)})^2 - (\mu_{g,\varsigma}^{(K)})^2]. \qquad (4)$$

Here $\langle S_{11}\rangle$ and $\langle S_{12}\rangle$ denote the orientational and transverse order parameters; $\langle S_{21}\rangle$ and $\langle S_{22}\rangle$ reflect the biaxiality of the film. The angle bracket implies that an orientation averaging has been taken with the orientation distribution $f(\Omega)$. For a uniaxial LC film, the resulting infrared absorbance is found to be [9–12]

$$A(\Phi = 90^\circ) = A_0\langle[-\cos\gamma\cos\phi\sin\beta + \cos\theta\sin\beta\sin\gamma\sin\phi + \cos\beta\sin\theta\sin\phi]^2\rangle$$

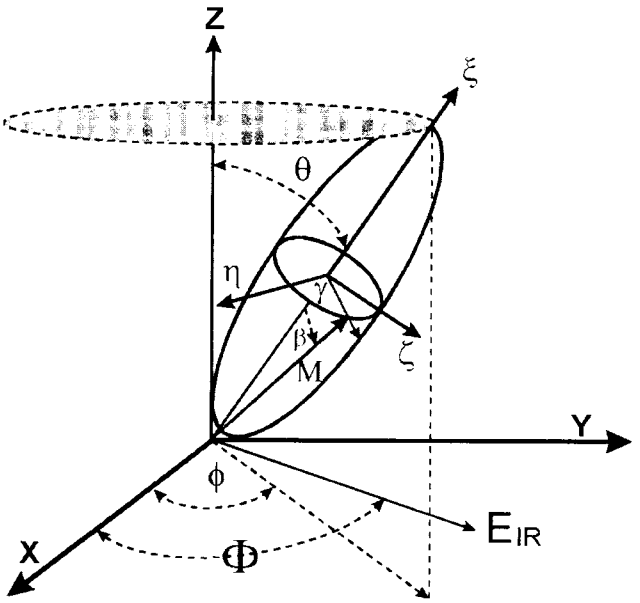

Figure 6. Schematic diagram showing the relationship between the molecular frame ($\xi\eta\zeta$) and the laboratory coordinates system (XYZ).

$$A(\Phi = 0^\circ) = A_0\langle[\sin\gamma\cos\theta\cos\phi\sin\beta + \sin\theta\cos\beta\cos\phi + \cos\gamma\sin\beta\sin\phi]^2\rangle. \qquad (5)$$

The infrared dichroic ratio DR can then be calculated with [7]

$$DR = A_X/A_Y = A(\Phi = 0^\circ)/A(\Phi = 90^\circ). \qquad (6)$$

The averaged orientation of LC molecules is taken to orient with the calculated director profile ($\theta(z)$, $\varphi(z)$) as shown in the inset of figure 1. This allows us to take into account the effect of the twist deformation in a twisted pi-cell by using equation (5). In the molecular frame ($\xi\eta\zeta$), the LC molecules are assumed to possess a degree of freedom in rotation about the molecular ξ-axis. A distribution function $f(\gamma)$ is introduced to describe the LC molecules rotating about the ξ-axis either freely with $f(\gamma) = 1$ or biasedly with $f(\gamma) = \cos^2\gamma$.

We found that the stretch modes associated with the LC core at 1502, 1606, and 2228 cm^{-1} can be successfully modeled with $\beta \sim 70^\circ$ and $f(\gamma) = \cos^2\gamma$. For comparison, the calculated results with a free rotation model are also presented in figure 5. Our results appear to indicate that the stretch modes associated with the LC core in the twisted pi-cell agree better with the biased rotation along the molecular long axis. This biased rotation could presumably originate from an interaction of LC molecules with the left-handed chiral dopants. The dichroic ratio of the FTIR peaks associated with the alkyl chains of the LC molecules shows no clear voltage dependence.

For these functional groups, a random distribution with $f(\gamma) = 1$ and $\beta \sim 54°$ is more appropriate in modelling their orientation distribution.

3.2. *Raman scattering spectroscopy of twisted LC pi-cells*

The Raman spectra taken with a laser polarized along the rubbing direction are presented in figure 7. As shown by figure 1, the director of the LC molecules is twisted by 180° along the Z-direction. The order parameter of the C=C stretching mode at $1606\,cm^{-1}$ is therefore decreased from 0.67 in a homogeneously aligned cell to 0.52 in a twisted pi-cell.

Several Raman peaks were observed to appear at 705, 790, 821, 957, 1177, 1240, 1285, 1606, and $2228\,cm^{-1}$, and are summarized in the table. The peaks at 705, 790, and $821\,cm^{-1}$ can be ascribed to the C–H out-of-plane wag on the core part of the LC molecule. The angular distortion of the LC core occurs at $957\,cm^{-1}$. The coupled motions of the C–C inter-core stretch and the C–H in-plane wag appear at 1177 and $1240\,cm^{-1}$; the coupling between the C–C intra-core stretch and C–H in-plane wag was found to be $1285\,cm^{-1}$. The C=C and C≡N stretching modes produce major peaks at 1606 and $2228\,cm^{-1}$.

In the C–H stretching region (see figure 8), two major peaks can be detected at $2851\,cm^{-1}$ (s-CH_2 stretch) and $2937\,cm^{-1}$ (f-CH_3). Unlike the vibrational features from the LC core, these C–H stretching peaks were found to increase with increasing applied voltage. This result also agrees with the FTIR result presented in figure 4(*b*) and suggests that the planes of the CH_2 groups are twisted by the electric field to yield a larger projection on the film surface for the a-CH_2 stretching.

It was found from simulation that the LC molecules tilt upward at near 90° when the applied voltage is higher than 4V. The high polar angle leads to a reduced

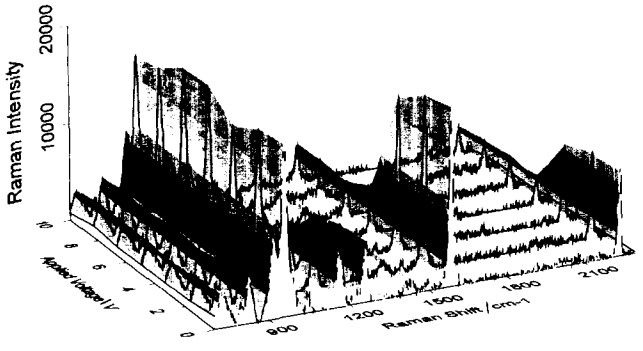

Figure 7. Raman spectra from a twisted pi-cell with varying applied voltage. The polarization of the incident laser beam is parallel to the rubbing direction of the pi-cell.

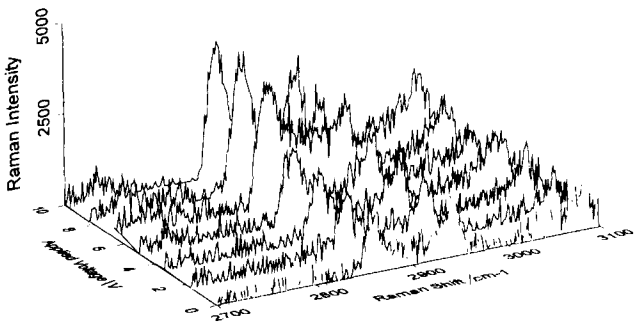

Figure 8. Raman spectra near the C–H stretching region from a twisted pi-cell with varying applied voltages. The incident laser beam is polarized along the rubbing direction of the pi-cell.

Raman intensity at $1177\,cm^{-1}$, $1285\,cm^{-1}$, $1606\,cm^{-1}$ and $2228\,cm^{-1}$ with an increasing applied voltage. This can be more clearly seen in figure 9.

3.3. *Field-induced reorientation of liquid crystal molecules in a twisted nematic pi-cell*

To evaluate how fast the twisted pi-cell responds to an electric field, we measured the optical transmittance of the cell with various switching frequencies. Modulated bipolar square waves with 50% duty cycle were employed as the driving field to acquire figure 10, which presents the results with the drive frequency varied from 50 Hz to 1 kHz. Compared with the measured T–V curve shown in figure 1, we found that the LC molecules do not return to the 0 V configuration as the drive frequency is higher than 100 Hz. As the drive frequency increases, the duration of the high field envelope (10 V) becomes shorter. At a sufficiently high drive frequency (e.g. 1 kHz), the repetitive high field envelope becomes shorter than the response times of the director. The tilt-up of the LC director driven by the high field and the relaxation back

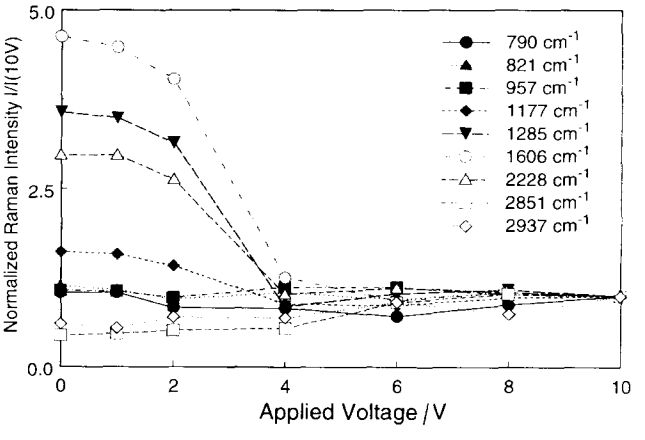

Figure 9. Normalized Raman peak intensities versus applied voltage. The Raman intensities are normalized to the values at 10 V.

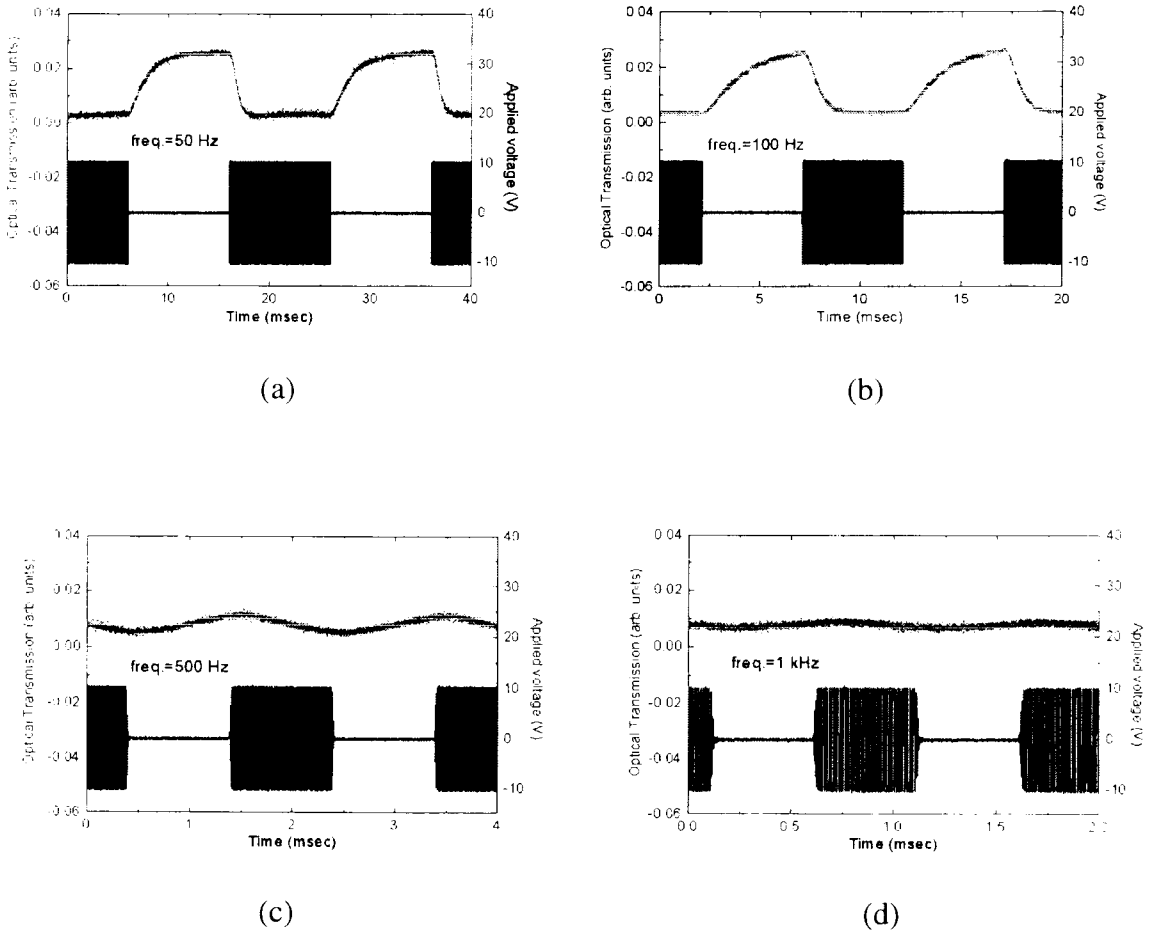

Figure 10. Optical transmission through a twisted pi-cell lying in a set-up of crossed polarizers and analyser. The rubbing direction of the cell was oriented at 45° relative to the transmission axis of the polarizer. The applied voltage was switched from 0 to 10 V at (*a*) 50 Hz, (*b*) 100 Hz, (*c*) 500 Hz, and (*d*) 1 kHz.

to the low pretilt configuration at 0 V do not have sufficient time for completion. By switching the voltage from 0 to 10 V, the liquid crystal molecules behave as in switching from 5 to 9 V at 500 Hz, and from 6 to 8 V at 1 kHz. The rise time (0% → 90%) of the optical transmittance was measured to be 6 ms and the decay time (100% → 10%) to be about 1.6 ms.

The transient Raman spectra taken from the LC cell during its field-induced switching are presented in figure 11. A modulated square wave at 500 Hz was applied to the cell. The 10 V amplitude spans from 0 to 1 ms and the 0 V extends from 1 to 2 ms.

The 790 cm^{-1} peak (marked grey), which has been attributed to the C–H out-of-plane wag on the LC core, is significantly enhanced when $t > 1$ ms. The rapidly changing polar angle of the LC molecules could play a role in yielding the enhanced out-of-plane C–H wag. Similar enhanced responses after switch-off were also found at the CH_2 and CH_3 stretching modes (not shown here), indicating that LC molecules do not respond to

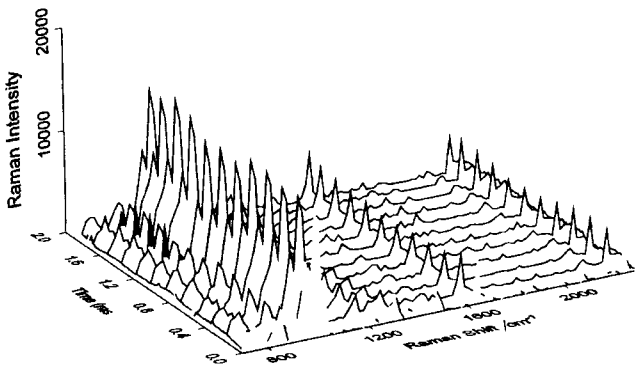

Figure 11. Raman spectra from a twisted pi-cell at varying time. The applied voltage is switched from 0 to 10 V at 0 ms, and 10 to 0 V at 1 ms. The incident laser beam is polarized along the rubbing direction of the pi-cell.

an external field like a rigid molecule. In figure 12, the applied voltage and the peak intensities at 790, 1606 and 2228 cm^{-1} in figure 11 are plotted as a function of

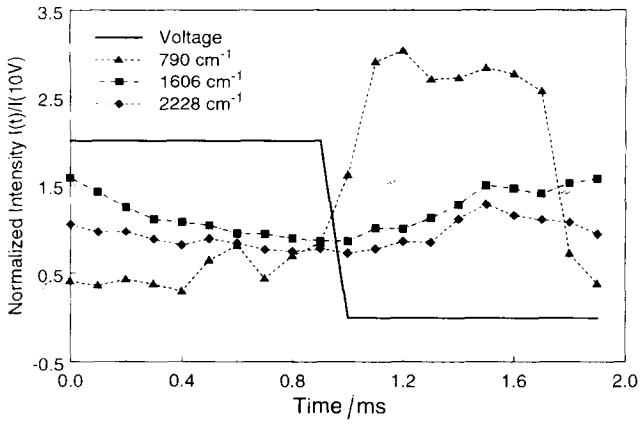

Figure 12. Normalized Raman peak intensities versus time. The applied voltage is switched from 0 to 10 V at 0 ms, and 10 to 0 V at 1 ms. The Raman intensities are normalized to the values at 10 V.

time. The observed field-induced intensity variations at Raman modes associated with the LC core are strikingly similar to figure 10, indicating the optical response of the pi-cell is dominated by the orientation dynamics of the LC core.

4. Conclusion

In conclusion, a twisted nematic liquid crystal pi-cell had been studied in detail by optical techniques including optical transmission measurement, polarized Fourier-transform infrared (pFTIR) absorption spectroscopy and Raman spectroscopy. From the pFTIR, the alignment of the LC molecules was revealed and was shown to exhibit a restricted rotation about the molecular long axis. The rise and decay times of the optical response in the twisted pi-cell to an external driving field can be smaller than 6 ms. The switching dynamics was further probed with time-resolved Raman spectroscopy. The vibrational activity of the C–H out-of-plane wag on the LC core was found to be enhanced during the switch-off period. Our data suggest that LC molecules in the twisted pi-cell do not rotate like a rigid molecule during the field-induced reorientation process. The methods used in this study yield valuable information about LC alignment and field-induced reorientation with molecular specificity.

We acknowledge financial support from the National Science Council of the Republic of China under grant NSC 89-2112-M-009-069. We are also indebted to Dr Chiou-Lien Yang for her generous supply of the LC material used in this study.

References

[1] Bos, P. J., Koehler, R., and Beran, K., 1984, *Mol. Cryst. liq. Cryst.*, **113**, 329.
[2] Miyashita, T., Kuo, C. L., and Uchida, T., 1995, *SID95*, 797.
[3] Nakamura, H., and Noguchi, M., 2000, *Jpn. J. appl. Phys.*, **39**, 6368.
[4] Yang, C.-L., and Chen, S. H., 2002, *Appl. Phy. Lett.*, **80**, 20.
[5] Hide, F., Clark, N. A., Nito, K., Yasuda, A., and Walba, D. M., 1995, *Phys. Rev. Lett.*, **75**, 2344.
[6] Hayashi, N., and Kato, T., 2001, *Phys. Rev. E*, **63**, 21 706.
[7] Delley, B., 1991, in *Density Functional Methods in Chemistry*, edited by J. K. Labanowski and J. W. Andzelm (New York: Springer-Verlag), pp. 101–108.
[8] Skupin, H., Kremer, F., Shilov, S. V., Stein, P., and Finkelmann, H., 1999, *Macromolecules*, **32**, 3746.
[9] Sigarev, A. A., Vij, J. K., Panarin, Yu. P., and Goodby, J. W., 2000, *Phys. Rev. B*, **62**, 2269.
[10] Jang, W. G., Park, C. S., and Clark, N. A., 2000, *Phys. Rev. E*, **62**, 5154.
[11] Jang, W. G., Park, C. S., Kim, K. H., Matthew, M. A., Glaser, A., and Clark, N. A., 2000, *Phys. Rev. E*, **62**, 5027.
[12] Kocot, A. Wrzalik, R., Orgasinska, B., Perova, T., Vij, J. K., and Nguyen, H. T., 1999, *Phys. Rev. E*, **59**, 551.